






Article

High-Resolution Analysis of Critical Minerals and Elements in Fe–Mn Crusts from the Canary Island Seamount Province (Atlantic Ocean)

Egidio Marino ^{1,2,3,*} , Francisco Javier González ¹ , Rosario Lunar ^{2,3}, Jesús Reyes ⁴, Teresa Medialdea ¹ , Mercedes Castillo-Carrión ⁴ , Eva Bellido ⁴ and Luis Somoza ¹ 

¹ Marine Geology Division, Geological Survey of Spain (IGME), Ríos Rosas, 23, 28003 Madrid, Spain; fj.gonzalez@igme.es (F.J.G.); t.medialdea@igme.es (T.M.); l.somoza@igme.es (L.S.)

² Mineralogy and Petrology Department, Geology Faculty, Complutense University of Madrid (UCM), Jose Antonio Novais, 2, 28040 Madrid, Spain; lunar@ucm.es

³ Geosciences Institute (IGEO-UCM-CSIC), Severo Ochoa 7, 28040 Madrid, Spain

⁴ Central Laboratories, Geological Survey of Spain (IGME), C/La Calera, 1, 28760 Tres Cantos—Madrid, Spain; j.reyes@igme.es (J.R.); m.castillo@igme.es (M.C.-C.); e.bellido@igme.es (E.B.)

* Correspondence: emarino@ucm.es

Received: 28 May 2018; Accepted: 27 June 2018; Published: 2 July 2018



Abstract: Two Fe–Mn crusts among 35 samples, from six seamounts in the Canary Island Seamount Province, were selected as representatives of the endpoint members of two distinct types of genetic processes, i.e., mixed diagenetic/hydrogenetic and purely hydrogenetic. High-resolution analyses pursued the main aim of distinguishing the critical elements and their association with mineral phases and genetic processes forming a long-lived Fe–Mn crust. The Fe–Mn crust collected on the Tropic Seamount is composed of dense laminations of Fe-vernadite (>90%) and goethite group minerals, reflecting the predominance of the hydrogenetic process during their formation. Based on high-resolution age calculation, this purely hydrogenetic crust yielded an age of 99 Ma. The Fe–Mn crust collected on the Paps Seamount shows a typical botryoidal surface yielding an age of 30 Ma. electron probe microanalyzer (EPMA) spot analyses show two main types of manganese oxides, indicating their origin: (i) hydrogenetic Fe-vernadite, the main Mn oxide, and (ii) laminations of interlayered busierite and asbolane. Additionally, the occurrence of calcite, authigenic carbonate fluor-apatite (CFA) and palygorskite suggests early diagenesis and pervasive phosphatization events. Sequential leaching analysis indicated that Co, Ni, Cu, Ba and Ce are linked to Mn minerals. Therefore, Mn-oxides are enriched in Ni and Cu by diagenetic processes or in Co and Ce by hydrogenetic processes. On the other hand, Fe-oxides concentrate V, Zn, As and Pb. Moreover, the evidence of HREE enrichment related to Fe-hydroxides is confirmed in the mixed hydrogenetic/diagenetic crust.

Keywords: ferromanganese crusts; high-resolution analysis; critical elements; co-chronometer; diagenesis; hydrogenesis; phosphatization

1. Introduction

Ferromanganese crusts (hereafter Fe–Mn crusts) grow on seamounts and plateaus worldwide, where currents are strong enough to keep the rock substrate clear of sediments. “Cobalt crusts” are defined as hydroxide/oxide deposits of cobalt-rich iron/manganese concretions formed by direct precipitation of minerals from seawater onto hard substrates [1]. The interest in these deposits began in the early 1980s when they were considered for the first time as a potential Mn, Co, Ni and Cu source [2–5]. The attention on this deposit rose when recent investigations highlighted that Fe–Mn crusts are also enriched in several critical metals and rare earth elements plus yttrium (REYs) [6–14].

Previous studies of Fe–Mn nodules and crusts showed that the enrichment in a specific metal, basically depends on the type of genetic process responsible for their growth. In this sense, diagenetic Mn nodules are normally enriched in Mn, Ni and Cu, but impoverished in Co, Fe, and in general REYs and platinum group elements (PGEs) [6,15–18]. Otherwise, Fe–Mn hydrothermal crusts and stratabounds are highly enriched in Mn or Fe, and rarely enriched in trace elements such as Zn, Ni or Ba, depending on the composition of the hydrothermal fluids and leached elements, with very low contents of REYs and PGEs [17–22]. Finally, Fe–Mn crusts of hydrogenetic origin are very enriched in Mn, Co, REYs, PGEs as well as in Ni, Ba, V, Mo, W, Nb, Tl, etc. [2,6,8,15,23–27].

Critical metals are used in a growing number of high and green emerging technologies as well as in different energy applications (Table 1 in [11]). The new emerging economies, such as the Indian, Brazilian and Chinese ones, have induced an increasing demand on these rare metals, but the exploited terrestrial deposits may be exhausted in the coming years. For this reason, the European Commission is promoting the Raw Materials Initiative within the Horizon 2020, which has pointed out 27 critical elements [28,29] including Co, V, Cd, Te, Ba, REY and PGEs. The motivation of the Raw Materials Initiative is to avoid the high dependence on imports and to ensure the supply of these raw materials. Advances in technology have encouraged mining companies to look to the oceans and start considering the exploration and exploitation of marine minerals. It is expected that by 2020, 5% of the world's minerals, for example cobalt, copper and zinc, and related critical metals as by-products, could be mined from the ocean floor (COM/2012/0494 final). In this sense, it must be mentioned that the International Seabed Authority [1], established in 2012 the regulation of prospecting and exploration for cobalt-rich Fe–Mn crusts in areas beyond national jurisdictions. At present, several exploration contracts for cobalt-rich Fe–Mn crusts on the Pacific and South Atlantic seamounts have been signed by different countries and companies.

Fine-scale dating, and chemical and mineralogical description of ferromanganese nodules and crusts have provided a significant insight into the exploration of potential ore deposits as well as archives for paleoenvironmental studies [30–34]. Ferromanganese deposits found on seamounts show micro-scale variation patterns of abundance and composition, in space and time for the seamounts, contributing to the development of robust models to explain the distribution of critical metals. Thus, the investigations should include detailed textural, mineralogical, geochemical and dating studies of individual layers within ferromanganese crusts from different depositional settings for two reasons: (1) to better evaluate the controls on the economic potential of seamounts ferromanganese deposits; and (2) for the selection of viable mine sites and the design of environmentally sound and efficient mining systems for the future.

In this work, we present, for the first time, a high-resolution analysis of two representative samples selected from up 35 Fe–Mn crust samples collected on the Canary Island Seamount Province (CISP). Based on previous studies [27], these two samples were selected by showing the most important geochemical differences. In this study, we depart from the assumption that these geochemical differences closely represent endpoint members between distinct genetic processes, i.e., mixed diagenetic and purely hydrogenetic Fe–Mn crusts [27]. Therefore, the high-resolution analyses of these end-members are aimed at evidencing how these two genetic processes affect the mineralogy of the Fe–Mn crusts and, furthermore, which mineral phases of the array of critical elements are enriched. In this way, the high-resolution analyses include mineralogical analysis (petrography, X-ray diffraction (XRD), high resolution transmission electron microscopy (HR-TEM), scanning electron microscope (SEM), electron probe microanalyzer (EPMA)), mineralogical-geochemical experiments (thermic treatment, cation exchange, sequential leaching), dating and chemical determinations by spectrometric techniques (X-ray fluorescence (XRF), inductively coupled plasma mass spectrometry (ICP-MS) and inductively coupled plasma atomic emission spectroscopy (ICP-AES)).

2. Geological and Oceanographic Setting

The study area is located southwest of the Canary Islands Archipelago, and ca. 100 km west off the African coast (Figure 1). The origin of the Canary Islands and CISP seamounts is still under debate. The earliest studies on the archipelago targeted a typical hot-spot evolution such as the Hawaii Islands with the eastern islands older than the western ones [35–38]. Further studies proved that volcanism depends on an anomalously shallow mantle upwelling that causes rising and extrusion of magma at more or less the same location, but not as a typical hot-spot track. Dating of the CISP seamounts has evidenced that the magma forming these seamounts has risen since the Early Cretaceous period, after the opening of the Atlantic Ocean [39]. $^{40}\text{Ar}/^{39}\text{Ar}$ ages range from the older Las Hijas Seamount and El Hierro Ridge (142 Ma and 133 Ma, respectively) to younger seamounts such as Palma Ridge or El Hijo (2 and 0.2 Ma, respectively). Therefore, the CISP can be considered as the oldest and most long-lived hot-spot track in the Atlantic Ocean. The relationship between the Mesozoic CISP seamounts and the Cenozoic Canary Islands is evidenced by their similar type of volcanism. Volcanism of the Canary Islands is typical of the oceanic islands, essentially alkali type with some subsequent magma evolution [40,41]. Studied samples recovered on CISP seamounts show a similar alkali composition [42,43], indicating therefore a common origin.

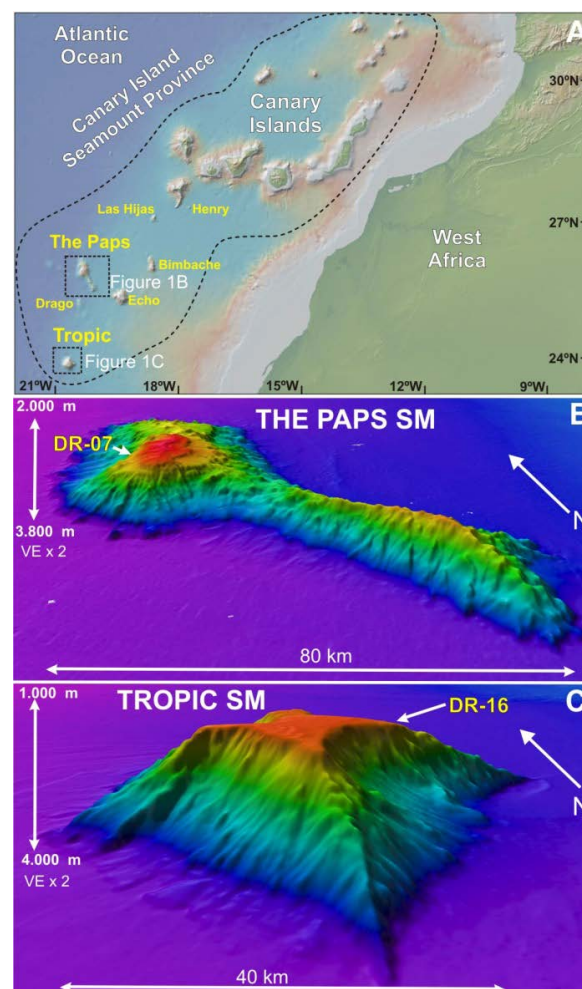


Figure 1. Regional setting of the Canary Islands Seamounts Province (CISP). (A) General view of the study area where the Canary archipelago and the most important seamounts of the southwest area of CISP are displayed; (B,C) Three-dimensional view produced with Fledermaus™ software and high-resolution bathymetry of the Tropic and The Paps seamounts. The position of the selected dredge hauls is indicated with arrows.

The CISP is formed by up to a hundred submarine hills and seamounts that extend over an area between 23–33° N and 13–21° W. Seamounts rise from ca. 5000 m depth up to 200 m depth. The summits are coated by crusts whose substrate rock consists of (altered) basalts, volcanic breccia and lapilli, carbonates and in some cases phosphorites. Since the 1990s, several expeditions (SONNE 83 cruise, METEOR cruise M 43, DRAGO0511 cruise; SUBVENT-1 cruise; SUBVENT-2 cruise) have reported the presence of extensive Fe–Mn crust deposits covering tops and flanks of the CISP seamounts [13,26,27,42–46].

The CISP has an important oceanographic regime of currents. According to the potential density of the mass waters, the water column can be divided into three main zones: the upper zone (0–100 m), the intermediate zone (100–1000 m) and the deep zone (1000–4000 m).

The upper zone is characterised by the Canary Current (CC), a southern branch of the Azores Current (AC). The intermediate zone is mainly composed of the North Atlantic Central Water (NACW) moving from north to south, and the slightly dense South Atlantic Central Water (SACW) which flows in the opposite direction. In this intermediate zone, the Mediterranean Outflow Water (MOW) and the Antarctic Intermediate Water (AAIW) are also present. The deepest bottom currents are essentially the North Atlantic Deep Water (NADW), moving up to 1500 m water depth, and the Antarctic Bottom Water (AABW), the densest water, that usually moves water masses across the seabed at 4000 m depth [47–51].

The CISP is also characterised by a thick Oxygen Minimum Zone (OMZ) ranging between 100 and 700 m with a core characterised by very low contents of dissolved oxygen ($<50 \mu\text{mol/kg}$) [52–55]. This thick OMZ in the eastern Atlantic is related to the high biological activity as a response to fertilization of the ocean by high inputs of Fe and P sourced from the Sahara dust [56–58]. The influence of this thick OMZ, which affects the growth rates of Fe–Mn crusts, has been evidenced in the CISP seamounts [27].

3. Materials and Methods

3.1. Samples

The samples analysed in this work were selected from a collection of 35 Fe–Mn crusts collected from six CISP seamounts. The Fe–Mn crusts were collected in 2011 using a rectangular rock dredge (2 m \times 0.8 m) on board the R/V Miguel Oliver during DRAGO0511 cruise. Samples and swath bathymetric data are part of the new extensive data set acquired for the Law of the Sea extended continental shelf (ECS) purposes. Sampling targets were selected after a previous seabed mapping using the Kongsberg-Simrad EM-302 multibeam echosounder [59]. 3D images of the seamounts were taken using Fledermaus™ software (Quality Positioning Services BV (QPS), Zeist, The Netherlands).

Two samples were selected from The Paps (DR07-8) and Tropic (DR16-13) Seamounts, respectively (Figure 1B,C) on the basis of previous studies of the Fe–Mn crusts [27], which highlighted important geochemistry differences, i.e., Mn contents (15 and 21.7 wt %, respectively), Fe (14.6 and 27.3 wt %), and especially in Co (3500 and 7000 $\mu\text{g/g}$), Ni (6000 and 3000 $\mu\text{g/g}$), Cu (1600 and 400 $\mu\text{g/g}$) and Ce (700 and 2100 $\mu\text{g/g}$) [27]. These differences indicate that both samples could represent endpoint members between mixed diagenetic and purely hydrogenetic Fe–Mn crusts.

The Paps Seamount displays in the swath bathymetry and 3D images (Figure 1B) a N-S ridge-like morphology with a narrow arm extending in a NW-SE direction. This seamount rises from 4400 m depth to 3000 m at the northern summit and extends over an area of 2150 km². Fe–Mn crusts were dredged on the northern flank (dredge samples DR07, DR09, DR10 and DR11) and on the southern arm (DR14) (Figure 1B). The sample selected for this study belongs to the DR07 dredge, collected in the northern sector of the seamount at 1860 m depth (Figure 1B). Calculated $^{40}\text{Ar}/^{39}\text{Ar}$ age in several feldspar micro-phenocrysts of the Paps Seamount gave a mean age of 91 Ma [39].

The base of the Tropic Seamount, found at 4300 m depth, occupies an area of 1530 km² (Figure 1C). This seamount of 3300 m in height shows typical guyot morphology with a “mesa”-type flat summit surrounded by steep flanks. In plain view, it shows a four-arm star caused by the action of landslide scars [59]. Two dredges were collected on this seamount: dredge DR15 on the southern arm at 2200 m depth and, dredge DR16 on the eastern arm at 1700 m depth. The sample selected for this study belongs to dredge DR16 (Figure 1C). The mean age of this seamount has been estimated as 119 Ma at the top of the seamount and around 80 Ma on the northern arm [39].

3.2. Laboratory Methods

Petrographic, mineralogical and geochemical methods were performed at the Central Laboratories of the Geological Survey of Spain (IGME), the Department of Crystallography and Mineralogy, Faculty of Geosciences (UCM) and the National Centre of Electronic Microscopy (CNME). Mineralogical identifications were performed by X-ray powder diffraction (XRD, Philips Analytical, Almelo, The Netherlands) based on 12 sub-samples. The equipment used included a PANalytical X'Pert PRO diffractometer, CuK α radiation, carbon monochromator and automatic slit (PTRX-004). The analytical conditions for the XRD were as follows: CuK α radiation at 40 kV and 30 mA, a curved graphite secondary monochromator, scans from 2–70° (2 θ), step size of 0.0170° (2 θ) and step time 0.5°/min. An analysis was conducted on a bulk sample at room temperature and also dried at 40, 100 and 300 °C. The cation exchange experiment (CEE) was used to verify the presence of phyllosilicates in crusts with interlayer regions accessible for cation exchange of K⁺ and Mg²⁺ ions as described by [60] and subsequently used by [17].

Scanning electron Microscope (SEM) images and analysis were obtained with a JEOL JSM 6335F (JEOL, Tokyo, Japan) with a cold (cathode) field-emission electron gun performed on up to 8 fragments of crusts. The SEM max resolution was 1.5 nm with 15 kV voltage at 4 mm distance. The backscattered electron detector worked with 2 nm resolution at 8 mm distance. The energy-dispersive X-ray spectroscopy (EDS, Oxford Instruments, Abingdon, UK) qualitative analysis was conducted with an Oxford Instruments, model: X-Max 80 mm² with a resolution of 127 eV to 5.9 KeV and performed with INCA software (ETAS GmbH, Stuttgart, Germany). This study was based mostly on the 58 SEM photomicrographs that were taken from these samples.

The high-resolution transmission electron microscope (HR-TEM) used was a JEOL JEM 3000F (JEOL, Tokyo, Japan) with a Schottky-type field emission electron gun at an accelerating voltage of 300 kV, 0.17 nm resolution. A micro-analysis system was implemented by an XEDS detector (OXFORD INCA) and an ENFINE spectrometer (resolution in energy of 1.3 eV). The study was carried out in 10 powdered sub-samples.

An electron probe micro-analyser (EPMA) was applied on polished thin sections using a Jeol JXA-8900M Electron Probe WDS/EDS Micro Analyser (JEOL, Tokyo, Japan), operating at 15–20 kV and 50 mA, operating at 15 EDS, equipped with four wavelength dispersion spectrometers in which these crystals were placed, as follows: channel 1: TAP; channel 2: LIF; channel 3: PETJ; channel 4: PETH. Standards included pure metals, synthetic and natural minerals, all from international suppliers. Back-scattered electron images were also obtained with this instrument. Profiles across crust samples were obtained to check the presence of compositional zoning and layer-by-layer growth rate and age determinations. Chemical EPMA determinations were carried out in 100 spot analyses in mineral phases, 183 and 292 layer-by-layer analysis in crusts DR07-8 and DR16-13, respectively. One hundred photomicrographs of mineralogical and textural features were taken with this instrument.

The major elements for both bulk Fe–Mn crusts were determined using X-ray Fluorescence (XRF, Philips Analytical, Almelo, The Netherlands), PANalytical's Magix equipment with a rhodium tube and Major software (PTE-RX-001 Ed. 3) and Irons protocol. The accuracy of the data was verified using international standard NOD-A-1, and precision based on duplicate samples was found to be better than $\pm 5\%$. Analytical conditions were 50 kV voltage and 50 mA. Na was measured using a VARIAN FS-220 atomic absorption spectrometer and loss on ignition (LOI) was determined by calcination

at 950 °C. ICP-AES (Varian Vista-MPX, Varian Inc., Palo Alto, CA, USA) was used to measure Nb, S and W in bulk samples. Samples were prepared with acid HF HNO₃ and HClO₄ digestion until completely dried and residual was diluted with ClH 10%. Other trace Elements Be, V, Co, Ni, Cu, Zn, As, Se, Mo, Ag, Cd, Sb, Ba, Tl, Pb, Th, U and REEs plus Y were measured with ICP-MS (AGILENT 7500 CE, Agilent Technologies, Santa Clara, CA, USA) with 3-acid and 4-acid digestion. The patterns obtained were compared with certified international standards (NOD-A-1, USGS, NBS, CANMET, BCS). The standard reference materials SO-1 (CCMET), GSP-1 (USGS) and BCR-1 (USGS) were used to test the analytical procedure for REY determinations.

Sequential leaching was adapted from [61], and according to [44] method for Fe–Mn crusts, essentially used for different acid digestions. Acetic acid at 10% concentration was used to extract carbonates, 1 M hydroxylamine hydrochloride was used to extract Mn oxides, concentrated HCl was used to extract Fe oxyhydroxides and finally concentrated HF was used to digest residual silicates. Every solution was analysed by ICP-AES for Al, Ca, Fe, K, Mg, Mn, Na, Nb, P, S and W; and by ICP-MS for Be, V, Co, Ni, Cu, Zn, As, Se, Mo, Ag, Cd, Sb, Ba, Tl, Pb, Th, U and REY.

Crust growth rates and ages were calculated by the empirical Co-chronometer method established by [62] which closely match isotopic determinations. The growth rate is (mm/My) = $0.68/Co_n^{1.67}$, where Co_n is (Co wt % × 50)/(Fe + Mn wt %). One limitation of this Co-chronometer method is that the equation does not measure possible hiatuses during the accretion process. Therefore, the calculated rates represent maximum values and the derived ages minimum values; if dissolution and re-precipitation take place can accumulate higher growth rates relative to diagenesis [63]. Multi-elemental spot analyses of Fe, Mn, and Co were carried out across two continuous profiles from the base to the edge of the crusts using electron probe microanalyzer (EPMA, JEOL, Tokyo, Japan) with a JEOL JXA-8900M Superprobe. Analysis is based on the study of 183 and 292 layer-by-layer analysis for the EPMA profiles of ferromanganese crusts DR07-8 and DR16-13, respectively.

The varimax rotated factor matrix was used to calculate different factors found in the study samples for Mn, Fe, Si, Al, K, Ca, Na, Mg, P, Co, Ni, Cu, Ce, Mo, V, Ba and W. DR07-8 factor was obtained with 183 layer-by-layer EPMA analyses while DR16-13 factor was obtained with 292 layer-by-layer analyses. More factors have been obtained by Varimax in both crusts but all of them have counts down to 5% and considered not representative by the statistical program. These non-representative factors have not been included in the factor list.

4. Results

4.1. Physical Properties, Textural Features and Mineralogy

4.1.1. Layering and Growth Patterns

Three main types of textures can be identified within the Fe–Mn crusts: (1) dense parallel laminations; (2) mottled to dendritic texture; and (3) columnar texture (Figures 2 and 3). Otherwise, light coloured thin laminations intercalated between these textures correspond to siliciclastic and carbonate detrital accumulation (coccolith, bioclasts) or authigenic phosphate minerals.

The Fe–Mn crust DR07-8 has a maximum thickness of 8 cm, showing a typical botryoidal surface with botryoids reaching diameters of 1–2 cm. This crust shows typical black colour with some dark brown layers, sub-parallel to the botryoidal surface (Figure 2A,B). Carbonate substrate rock of crust DR07-8 consists of semi-consolidated limestone with abundant foraminifera and scattered small clasts of volcanic rocks. The layered structure is composed of four main layers with an average thickness of ≈ 10 mm each (Figure 3A,B). The base of the crust (Layer 4) consists of thin dense laminations overlying the substrate. The other three layers consist of a porous mottled to dendritic base with dense sub-layers at the top, less than 0.5 mm in thickness.

The Fe–Mn crust DR16-13 has a mean thickness of 9 cm without botryoids on its surface. It is composed of dark brown to black layers with a smooth metallic to submetallic lustre surface, and red coloured areas caused by alteration (Figure 2C,D). The altered basalt breccia that composed the substrate of this crust is replaced by pervasive phosphatization. This crust shows a clear layering structure caused by parallel dense lamination. It has also been possible to differentiate four layers. The lowermost layers 3 and 4 are thicker (up to 2 cm) than the uppermost 1 and 2 (Figure 3C,D). Lamination is essentially composed of parallel and columnar growth patterns. In this sample, it is also possible to determine a rhythmic behaviour with alternation of porous mottled to dendritic areas at the base and a dense lamination in the uppermost part of the first three layers. Layer 4 is essentially formed by a thicker succession of dense parallel laminations.

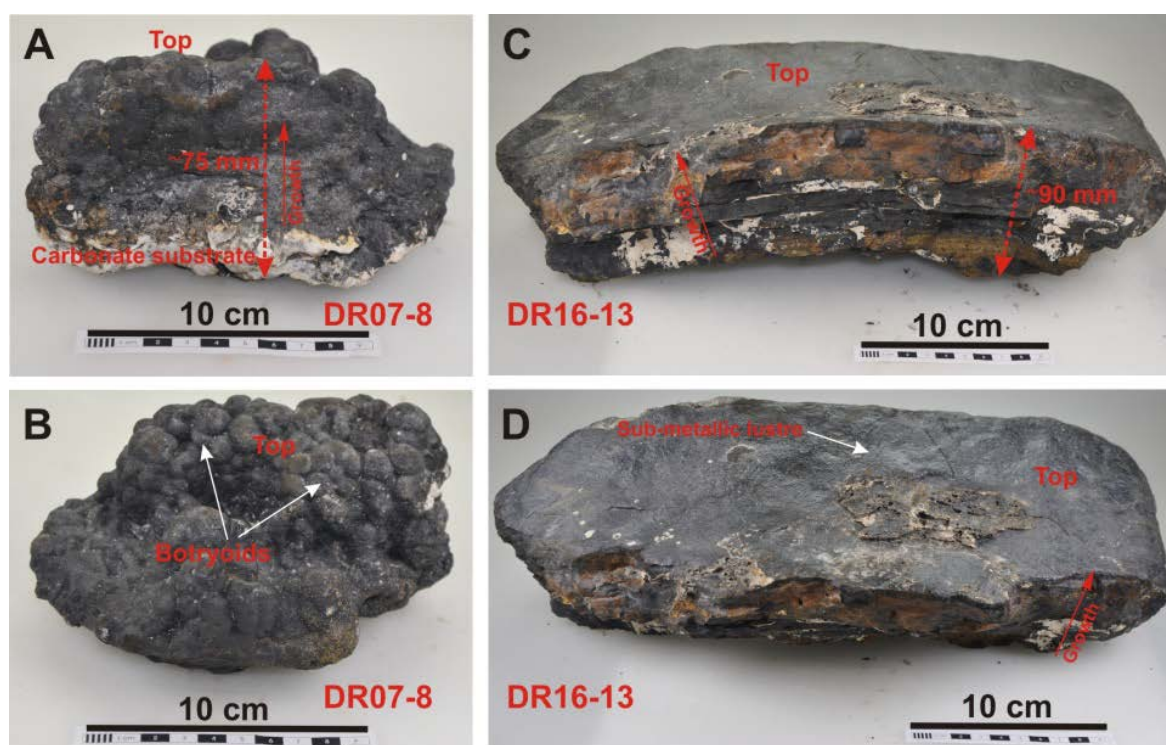


Figure 2. Images of the selected Fe–Mn crusts. (A,B) Frontal and upper view of DR07-8 collected from The Paps Seamount and (C,D) of DR16-13 collected from the Tropic Seamount. Both crusts show a different morphology; crust DR07-8 is mainly botryoidal while crust DR16-13 shows a more planar shape.

Under the petrographic microscope, these layers are composed of several types of Fe–Mn oxy-hydroxide growth patterns (Figure 4). These oxy-hydroxides are observed as isotropic, low reflectivity and low to no pleochroic micro-crystalline mosaics (Figure 4). Crust DR07-8 is composed of three main types of oxy-hydroxides growth patterns and re-placement textures related to three different processes (Figure 4A): (a) Dense sub-parallel to columnar growths of oxy-hydroxides as can be seen in the uppermost part; (b) Pervasive phosphate replacements and oxy-hydroxide re-nucleation in the middle; and (c) Several bright (diagenetic) laminations, especially abundant in the lower part of the layers. In contrast, crust DR16-13 shows only oxy-hydroxide growth patterns, i.e., columnar, dense sub-parallel and mottled to dendritic with no evidence of phosphatization or diagenesis (Figure 4B).

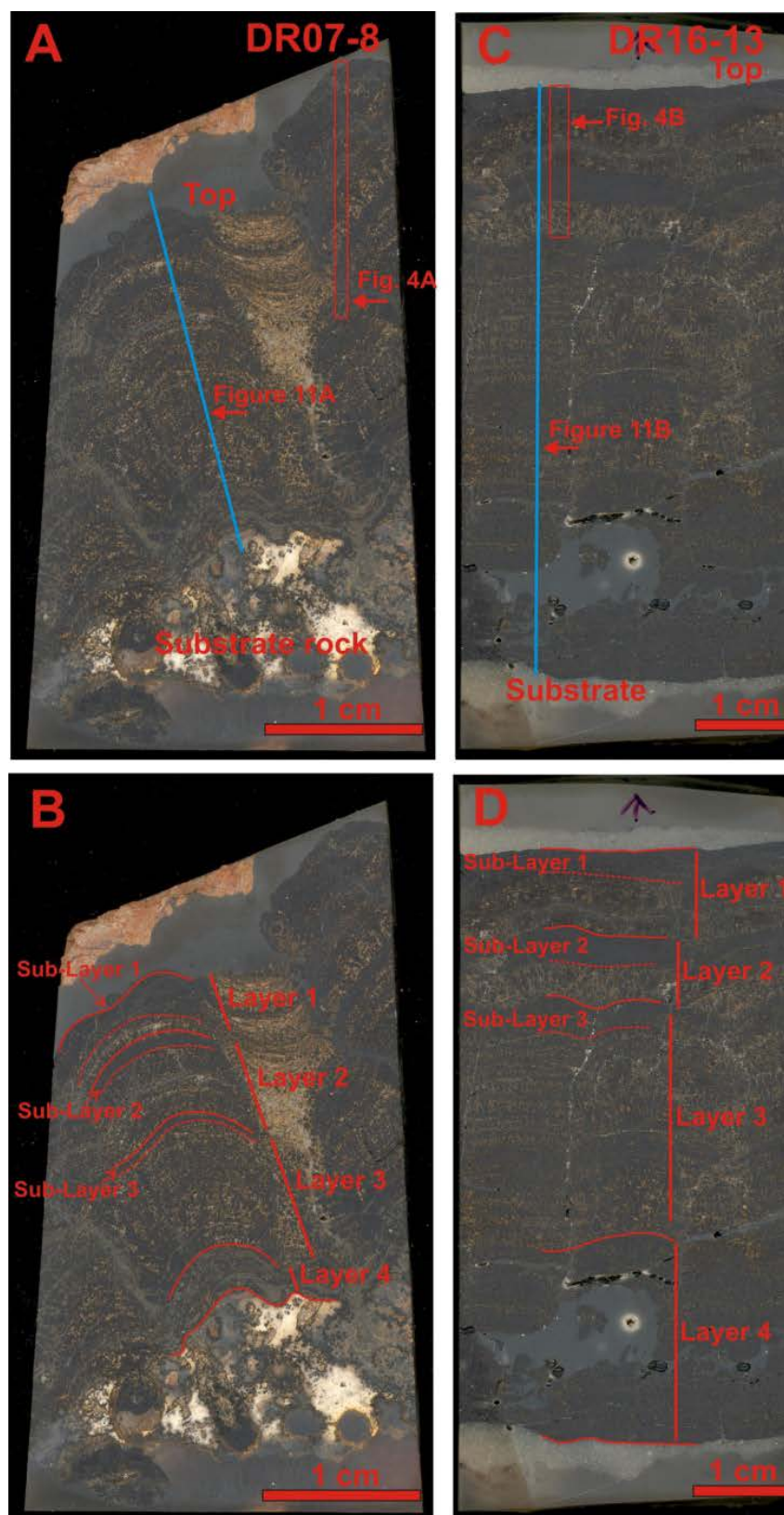


Figure 3. Cross polished section of the study crusts (A,B) DR07-8 and (C,D) DR16-13 which shows four main layers. Layers 1, 2, 3, 4 and sub-layers clearly visible in visu. The position of the layer-by-layer transect and continuous profile image obtained by optical microscopy is also marked.

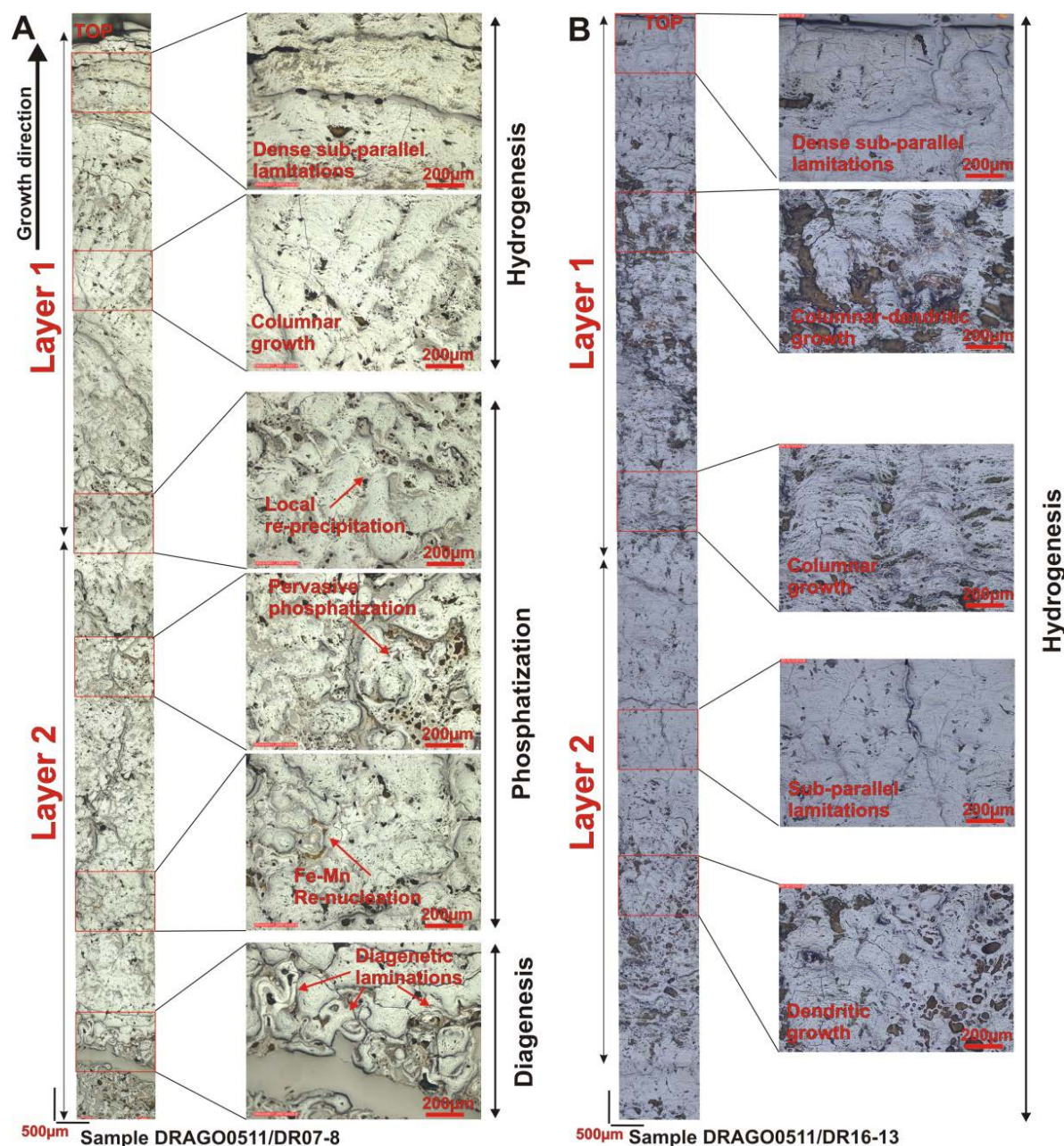


Figure 4. Representative sections under the petrographic microscope in continuous profiles. (A) profile section of crust DR07-8 and (B) profile section of crust DR16-13. Zoomed-in views represent specific interesting areas in which structures have been differentiated: (1) dense sub-parallel, (2) dendritic-mottled or (3) columnar growth. Several bright laminations (diagenesis) have also been recognised together with the presence of pervasive phosphatization bounded with dissolution and re-nucleation of Fe–Mn oxyhydroxides.

4.1.2. Mineralogy

XRD mineralogical analyses are summarised in Table 1. Analysis of bulk samples shows that major minerals are essentially Fe–Mn oxy-hydroxides: Fe-vernadite, 7 and 10 Å manganates and goethite group minerals (Figure 5). Accessory minerals are quartz, feldspar, calcite and less frequently, carbonate fluor-apatite (CFA) (Figure 5).

Table 1. XRD mineralogy of crystalline phases from CISP Fe–Mn crusts DR07-8 and DR16-13. Major > 25%; Minor < 10%. The back color is to differentiate both samples.

Sample	Type	T (°C)	Major Minerals	Minor Minerals
DR07-8	Bulk	40	Goethite, δ -MnO ₂ (Fe-vernadite, asbolan, todorokite, birnessite)	Quartz, anorthoclase, Carbonate-fluorapatite
	Bulk	100	Goethite, δ -MnO ₂ (Fe-vernadite, asbolan, todorokite, birnessite)	Quartz, anorthoclase, Carbonate-fluorapatite
	Bulk	300	Goethite, Hematite	Quartz, anorthite sodian, δ -MnO ₂ (Fe-vernadite)
DR16-13	Bulk	40	Goethite, δ -MnO ₂ (Fe-vernadite, birnessite)	Feroxyhyte
	Bulk	100	Goethite, δ -MnO ₂ (Fe-vernadite, birnessite)	Feroxyhyte
	Bulk	300	Goethite, Hematite	δ -MnO ₂ (Fe-vernadite, birnessite)

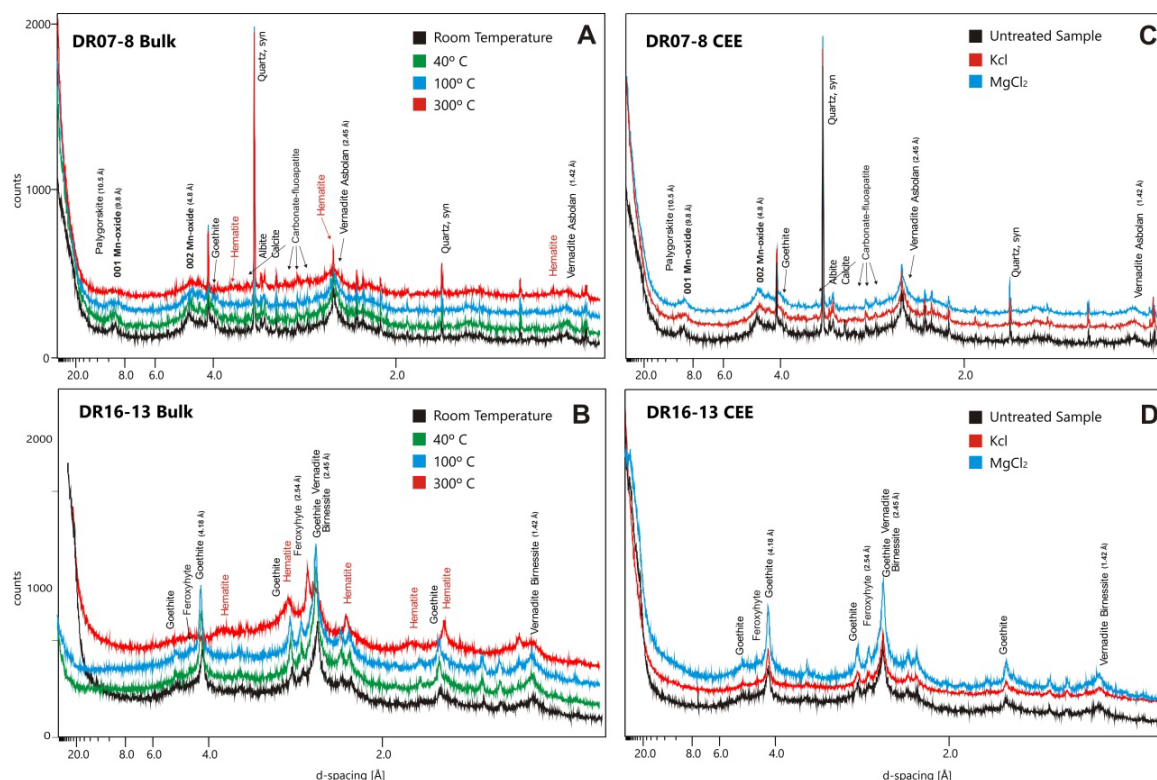


Figure 5. (A,B) XRD patterns of studied Fe–Mn crusts. Fe-oxhydroxides are represented in both crusts essentially by goethite and feroxyhyte. Mn minerals recognised are Fe-vernadite overlapping with birnessite. In DR07-8, it is also possible to recognise a 10 Å phyllosilicate (probably buserite/asbolane). Crystalline quartz, calcite, authigenic carbonate-fluorapatite and palygorskite are also observed in this sample. Thermic studies show the formation of hematite in both samples after drying at 300 °C; (C,D) CEE study does not show the presence of phyllosilicates with accessible interlayer regions.

The Fe oxyhydroxides represented in both crusts are essentially the same, i.e., goethite and feroxyhyte with their maximum reflection at 4.18 and 2.54 Å, respectively (Figure 5A,B). Otherwise,

Mn-minerals are different in both crusts. In DR07-8, busserite/asbolane at 9.8 Å intergrowths with Fe-vernadite at 2.45 Å is identified. In DR16-13, only Fe-vernadite overlapping with other Mn minerals, such as birnessite, is identifiable.

The XRD patterns of the DR07-8 crusts show characteristic reflections mainly corresponding to the occurrence of diverse Mn-oxides minerals (Figure 5A). Thus, the reflection identified around 9.8 Å (001 reflection) is attributed to todorokite, even though it could also correspond to disordered Fe-vernadite or busserite (Figure 5A). In this sense, reflection at ~4.8 Å is identified as (002) reflection of the same mineral [17,18]. Furthermore, Fe-vernadite is also detected around 2.45 and 1.42 Å, overlapping with other oxy-hydroxides such as asbolan, birnessite and goethite, and with secondary reflections of quartz. Goethite group minerals are the second in abundance in this crust. Their reflections are identified around 4.18 and 2.54 Å (Figure 5A). Minor amounts of detrital minerals are represented by quartz and feldspar (probably albite and orthoclase). Crystalline minerals such as calcite, carbonate fluor-apatite (CFA) and authigenic palygorskite are also recognised in this sample.

Sample DR16-13 shows a much more simple XRD pattern, where the Fe-vernadite is clearly the main Mn-mineral at 2.45 and 1.42 Å, but also in the broad reflection at 4.9 Å overlapping with goethite (Figure 5B). In this sense, goethite group minerals, essentially goethite and feroxyhyte, are also the unique minerals clearly recognizable in the XRD analysis. This crust does not yield detrital minerals such as quartz or feldspar (Figure 5B).

4.1.3. Thermic Treatment and CEE Experiments: Changes in Mineralogy

Changes in mineralogy were detected as samples were dried at different temperatures. XRD patterns (Figure 5A,B) show minerals after drying the sample at room temperature, 40, 100 and 300 °C. At 40 and 100 °C, both XRD patterns do not show any drastic changes. However, after drying at 300 °C, they change abruptly. Firstly, the ~10 Å and ~5 Å reflections, corresponding to phyllosulfates, and the 2.45 Å reflection of Fe-vernadite start to collapse. Secondly, the highest reflection at 4.2 Å also starts to collapse, being replaced by a reflection typical of hematite (Figure 5A). The same behaviour for thermic treatment of goethite has been found by several authors [64–66].

CEE experiments were used to identify whether the phyllosulfates of the studied crusts allow the incorporation of cations in their interlayer region. In this sense, samples treated with KCl would incorporate K⁺ cations showing a shift of the main peak from 10 to 7 Å. Otherwise, the treatment with MgCl₂ would incorporate bigger cations (Mg²⁺) with a shift of the peak position back to 10 Å. The peak position of 10 Å phyllosulfate in sample DR07-8 does not experience changes neither with the addition of KCl nor with the subsequent treatment with MgCl₂. At the same time, it has not been possible to identify shifting or newer reflections caused by this experiment in sample DR16-13 (Figure 5C,D). This experiment proves that turbostratic vernadite, a phyllosulfate with cation exchange power, is not present in the analysed crusts.

4.1.4. Scanning Electron Microscopy (SEM) and High-Resolution Transmission Electron Microscopy (HR-TEM) Analysis

SEM analyses of the crusts show very low crystallinity of Fe–Mn oxy-hydroxides, displaying only micro-aggregates morphologies (Figure 6). Thus, Fe–Mn oxy-hydroxides are observed forming micro-botryoidal surfaces which cover the previously formed minerals, cavity walls or detrital minerals and bioclasts (Figure 6A). The Fe–Mn oxy-hydroxides forming botryoids show radial and globular aggregates integrated by acicular micro-crystals of nanometre dimensions with “clay-like” morphologies (Figure 6B,C). Sample DR07-8 contains more detrital grains, represented by aluminium silicates (quartz and feldspar essentially), and bioclasts composed of fragmented coccoliths and foraminifera, included in the oxide laminations (Figure 6C,E). In contrast, sample DR 16-13 shows less detrital input but a higher rate of well-preserved coccoliths. Some rounded detrital quartz is also identified, sometimes covered by a Fe–Mn patina of very small acicular crystals (Figure 6B,D). Otherwise, tubular, fusiform, rod-shaped and chain-like forms indicate the occurrence of microbes at

the interspace voids of Fe–Mn oxy-hydroxide aggregates (Figure 6E). Acicular Fe–Mn oxide crystals also cover the walls of vacuoles or foraminifera (Figure 6F).

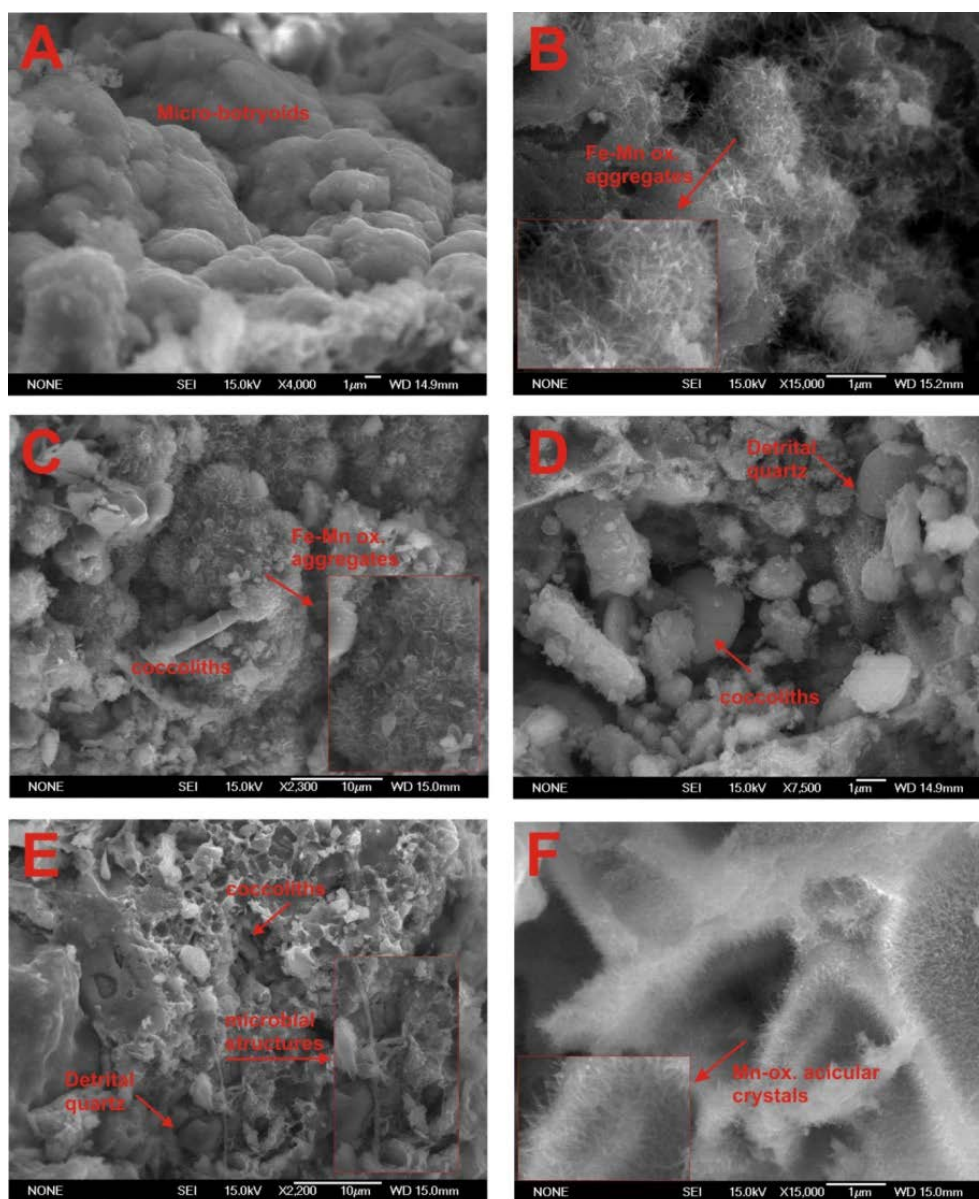


Figure 6. SEM photomicrography. (A) Micro-botryoidal morphology (B,C) Acicular micro aggregates of Fe–Mn minerals forming rounded shapes and sometimes covering other minerals or bio-clasts (F). (C,D) Detrital grains, coccoliths and (E) Biological tubular structure identified crossing through the Fe–Mn oxides.

HR-TEM analyses of the Fe–Mn crusts show the occurrence of very few mineral species with recognizable crystallographic planes, confirming the low crystallinity of Fe–Mn oxy-hydroxides (Figure 7). In this way, a great number of globular mineral aggregates with very low crystallinity are imaged, but only few crystal planes are well developed (Figure 7A,E).

In crust DR07-8, several 9–10 Å phylломanganates displaying high contents of Mn (up to 50 wt % for semi-quantitative analysis), Mg (14 wt %) and Ni (2.6 wt %) but low Fe (around 10 wt %) are identified (Figure 7B). In this way, Fe-vernadite (~7–8 Å cell space) is identified by its low crystallinity bearing high content values of Mn (50 wt %), Fe (~20 wt %) and Co (1 wt %), but low Mg (8 wt %)

(Figure 7C). The occurrence of goethite is also evidenced by its ~ 4.5 Å cell space (Figure 7B), by displaying regular planes, and by its high content in Fe (up to 80 wt %) but low contents of Mn (1–2 wt %). A phyllosilicate, probably palygorskite (Figure 7D), is also recognised based on its 10–11 Å cell space with very high contents of Si (up to 60 wt %) and Al (up to 15 wt %), but very low contents of Fe (19 wt %) and Mn (4 wt %).

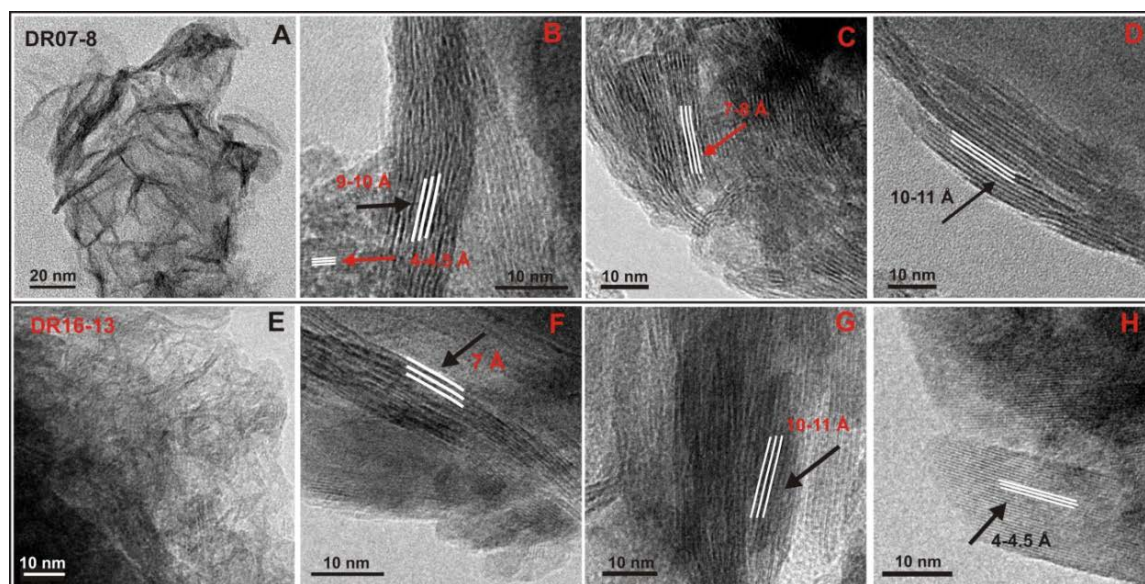


Figure 7. High resolution TEM photomicrographs. (A,E) Fe–Mn aggregates with very low crystallinity and few recognizable crystal planes. (B) Distinguishable 10 Å lattice fringes corresponding to 10 Å phyllosilicates (buserite/asbolane). (C,F) identified d-spacing belonging to vernadite/birnessite (7 Å) and (B,H) to goethite (around 4.2 Å). (D,G) lattice fringes corresponding to palygorskite (10–11 Å).

In the sample DR16-13, the unique Mn-mineral identified corresponds to a very low crystalline Fe-vernadite displaying a 7 Å cell spacing (Figure 7F). This vernadite shows the same contents of Mn (up to 50 wt %), higher in Fe (up to 30 wt %), Co (up to 1.5 wt %), and lower in Mg (2.5 wt %) in comparison to Fe-vernadite identified in DR07-08 crust. Goethite was picked in most of the analysis points overlapping the Fe-vernadite. HR-TEM images of goethite show a ~ 4.5 Å spacing with regular continuity, and similar elemental contents of goethite in crust DR07-8 (Figure 7H). Furthermore, some phyllosilicate crystals (palygorskite), showing similar elemental contents of Si (up to 58 wt %), Al (up to 20 wt %) and Mg (7 wt %) as those from sample DR07-8 but with slightly lower contents of Fe (14 wt %), and not bearing Mn (down to 0.5 wt %), are imaged with a spacing of ~ 10 Å (Figure 7G).

4.2. Geochemistry

4.2.1. Bulk Chemistry

Bulk chemical composition of the Fe–Mn crusts is summarised in Table 2. Crust DR16-13 with a Mn/Fe ratio of 0.78 is characterised by higher Fe and Mn contents (28 vs. 22 wt %, respectively) than crust DR07-8 (14.6 vs. 15 wt %, respectively), showing a Mn/Fe ratio of 1. Crust DR16-13 also shows relatively lower contents of detrital elements such as Si (1.7 vs. 8.6 wt %), Al (0.7 vs. 3.5 wt %) and Mg (1 vs. 2.7 wt %) regarding crust DR07-08. Both crusts are also moderately enriched in Ti (0.7 vs. 0.6 wt %), but crust DR16-13 is clearly depleted in Ca (2.5 vs. 5.8 wt %) and P (0.5 vs. 1.6 wt %) regarding crust DR07-08. This crust is enriched in Ca due to the presence of CFA and the nature of the carbonate substrate rock of this crust. As occurs with most of Fe–Mn crusts, silica filiation elements (Si, Al, K, Mg, Na and Ca) are depleted in terms of the mean crustal composition [67] (Figure 8).

Table 2. Chemical composition of the studied CISP Fe–Mn crusts. Bulk analysis and each sequential leaching fraction extracted during the experiment are represented. <D.L.: below detection limit. -: no data. Carb. = carbonates, Mn-Ox. = Mn-oxides, Fe-ox. = Fe oxyhydroxides, Silic. = silicates. The back color is to differentiate both samples.

SAMPLE	DR07-8 (Bulk)	DR07-8 (Carb.)	DR07-8 (Mn-ox)	DR07-8 (Fe-ox)	DR07-8 (Silic.)	DR16-13 (Bulk)	DR16-13 (Carb.)	DR16-13 (Mn-ox)	DR16-13 (Fe-ox)	DR16-13 (Silic.)
Fe (wt %)	14.6	0.01	1.33	11.71	0.35	28	<0.1	1.79	17.13	0.17
Mn	15	0.01	13.82	0.34	< 0.1	21.7	<0.1	17.97	0.48	<0.1
Mn/Fe	1.03	-	-	-	-	0.78	-	-	-	-
Si	8.6	-	-	-	-	1.7	-	-	-	-
Al	3.5	0.14	0.05	1.14	0.83	0.7	0.03	0.03	0.33	0.28
Ca	5.8	1.74	0.09	0.01	0.03	2.5	1.71	0.17	0.01	<0.1
Ti	0.6	<0.1	<0.1	0.44	0.04	0.7	<0.1	<0.1	0.32	0.02
K	0.6	0.17	0.04	0.02	0.23	0.3	0.17	0.04	<0.1	0.10
Mg	2.7	0.91	0.27	0.13	0.09	1.1	0.75	0.07	0.10	0.04
P	1.6	0.01	<0.1	0.40	0.03	0.5	<0.1	<0.1	0.19	0.05
Na	1.2	1.26	0.01	0.02	0.13	1.3	0.66	0.01	<0.1	0.01
LOI	22.87	-	-	-	-	27.15	-	-	-	-
Co (µg/g)	3218	0.77	2993.01	99.71	0.65	5530	1.13	5114.42	110.98	0.47
Ni	4796	224.95	4188.57	313.69	3.53	3285	151.09	2505.50	333.66	<D.L.
V	777	0.46	412.18	310.31	5.53	1170	0.31	607.12	427.70	3.22
Cu	1239	72.45	676.86	413.24	7.30	696	22.90	205.48	376.95	2.40
Be	8.2	1.35	0.33	4.74	0.14	12.24	1.50	1.14	6.58	<D.L.
S	3135	2164	580	239	< D.L.	3693	2463	578	83	13
Ba	1067	22.93	779.21	116.73	56.75	2034	16.15	1575.73	196.95	22.61
Zn	626	58.93	258.15	197.44	6.93	789	44.34	273.86	313.49	6.64
As	322	0.71	2.71	273.65	2.47	522	0.56	7.11	398.94	2.43
Mo	270	<D.L.	5.51	240.96	1.80	670	<D.L.	14.58	572.58	1.89
Nb	67	0.11	<D.L.	63.3	4.6	23	0.1	<D.L.	13.3	1.4
Se	22.7	1.48	9.96	13.06	0.15	40	1.24	23.47	16.61	0.04
Ag	0.16	<D.L.	<D.L.	<D.L.	0.11	0.2	<D.L.	<D.L.	<D.L.	0.18
Cd	5.3	0.28	4.23	<D.L.	<D.L.	1.8	<D.L.	1.39	<D.L.	<D.L.
Sb	47.7	<D.L.	0.22	22.73	1.26	81	<D.L.	0.13	58.80	1.16
Tl	112	22.61	81.79	12.00	0.39	142	16.68	106.08	12.84	0.30
Pb	976	<D.L.	77.53	989.54	3.56	1586	<D.L.	160.54	1450.74	2.23
Th	25.4	<D.L.	<D.L.	28.98	0.82	64	<D.L.	<D.L.	69.49	0.71
U	11	4.03	0.14	7.09	0.12	11.3	4.37	0.14	6.45	<D.L.
Y	225	6.91	57.7	43.9	0.73	173	3.84	77.05	33.05	0.305
La	142.8	6.52	82.95	33.8	1.73	304	5.585	215	49.8	0.585
Ce	938	1.11	459.5	363	3.055	2079	0.565	1243.5	583.5	1.38
Pr	30.6	1.135	12.5	12.2	0.32	73	1.11	37.35	23	0.095
Nd	126	5.435	47.95	55.2	1.095	286	5.245	141	101	0.32
Sm	27.3	1.215	7.935	14.2	0.175	59.2	1.205	24.55	25.65	0.065
Eu	6.9	0.315	1.96	3.51	0.06	13.8	0.305	5.76	5.815	0.02
Gd	33.2	1.62	11.7	15.65	0.15	59.4	1.37	28.6	21.5	0.055
Tb	4.88	0.2	1.57	2.54	0.02	8.4	0.16	3.885	3.35	0.01
Dy	30.3	1.115	9.505	15.8	0.14	46.6	0.825	21.35	18.7	0.055
Ho	6.3	0.22	2.09	3.16	0.03	8.7	0.145	4.065	3.315	0.01
Er	18.4	0.6	5.95	9.57	0.1	23.5	0.385	10.85	9.33	0.04
Tm	2.6	0.07	0.8	1.49	0.02	3.3	0.045	1.41	1.46	0.01
Yb	16.9	0.455	4.54	10.04	0.105	20.4	0.27	8.095	9.65	0.04
Lu	2.7	0.08	0.75	1.555	0.02	3	0.045	1.215	1.4	0.01

Both crusts, DR07-8 and DR16-13, show elevated contents of most of the trace elements defined as strategic and critical. The highest contents correspond to Co (3200 and 5500 µg/g, respectively), Ba (1000 and 2000 µg/g), Ni (4800 and 3200 µg/g), V (750 and 1100 µg/g), Cu (1250 and 700 µg/g), Mo (270 and 670 µg/g), Zn (600 and 790 µg/g) and Pb (1000 and 1600 µg/g). The total concentration of potential ore metals (Cu, Co, Ni, V, Zn and Mo) is quite similar, being 1.1 and 1.2 wt %, respectively. Furthermore, the contents of Co, Ni, Mo and Cu are between 100 and 1000 times enriched, regarding the standard contents of the continental crust [67] (Figure 8).

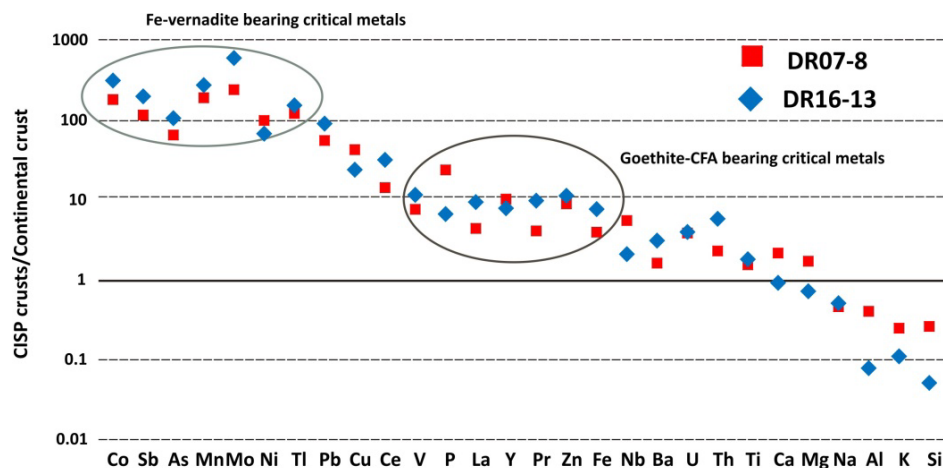


Figure 8. Element enrichment diagram for the composition of both studied crusts relative to the composition of the mean continental crust [67]; Mn-oxide (Fe-vernadite) bearing elements (Co, Ni, Mo and Ti) have been evidenced, in contrast with the Fe-oxyhydroxides and CFA bearing elements, (P, Y, V and Zn). Both crusts are depleted in aluminum-silicate elements.

At the same time, REYs are also enriched within these ferromanganese crusts (Table 2). Both crusts show similar REY patterns, i.e., enriched LREEs regarding HREEs. However, some differences between these two crusts can be identified considering their element concentration. Thus, sample DR07-8 shows lower contents of LREEs, MREEs and especially in La (143 $\mu\text{g/g}$), Ce (940 $\mu\text{g/g}$) and Nd (126 $\mu\text{g/g}$) (Figure 9A). On the other hand, in sample DR16-13, these elements show remarkably higher values (up two times) in La (300 $\mu\text{g/g}$), Ce (2000 $\mu\text{g/g}$), and Nd (290 $\mu\text{g/g}$) (Figure 9A). However, contents in HREEs are quite similar in these two crusts, showing their highest contents of Dy (30 and 47 $\mu\text{g/g}$, respectively), Er (19 and 23 $\mu\text{g/g}$), and Yb (17 vs. 20 $\mu\text{g/g}$).

The normalizing REY contents of the Fe–Mn crust regarding PAAS (Post-Archean Australian Shale) are shown in Figure 9B. Both patterns show a prominent Ce-positive anomaly which is related to the hydrogenetic origin of the crusts. The enrichment in LREEs and MREEs of crust DR 16-13 is also clearly depicted in the normalised REY diagram (Figure 9B).

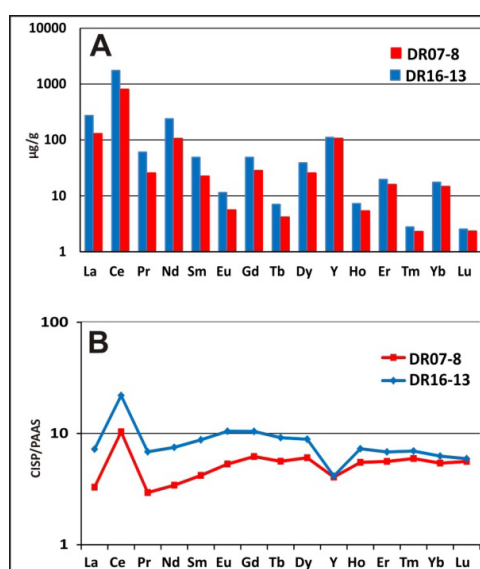


Figure 9. (A) Comparative graphic of the total concentration of REYs in both studied crusts; (B) PAAS normalised REYs plots for studied Fe–Mn crusts. PAAS from [68].

4.2.2. Chemistry of Mineral Phases after Leaching Experiments

Sequential leaching has been carried out in order to know which minerals mostly concentrate the different strategic and critical elements. The result of sequential leaching is shown in Table 2. Both DR07-8 and DR16-13 crusts display very low concentrations in Ca and Mg (bound to carbonates), that are leached in the first step together with S. This carbonate solution does not have high concentration of any other element; only Ni and Cu show minor contents (<300 µg/g). The second leaching step represents all Mn minerals that are in samples; ICP AES results show Mn concentrations of 14 and 18 wt %, respectively. This solution has a greater concentration of Co (3000 and 5200 µg/g) and Ni (4200 and 2500 µg/g) for both crusts, but shows different behaviour in the other strategic elements. Cu and Zn show the opposite behaviour; they are enriched in the Mn oxide step of DR07-8, but are slightly less enriched in the same step of DR16-13. Ba (780 and 1580 µg/g) is also enriched in Mn solution together with V (410 and 610 µg/g) and Tl (82 and 106 µg/g). The third leaching step concentrates Fe-oxyhydroxides and has Fe contents of 12 and 18 wt %, respectively. This solution concentrates other strategic elements such as Mo (241 and 573 µg/g), Sb (23 and 59 µg/g) and Pb (990 and 1450 µg/g). The last solution collects residual silicates showing a high concentration, essentially of aluminium silicates Al, K, and residual Ca, Mg and Na.

REEs plus Y have also been analysed in leached solutions to know which of the four separated phases are concentrated (Table 2). The results show that carbonates and residual solutions have very low content of REY with concentrations just at the detection limit. REY elements are concentrated in the manganese and iron oxides solutions but with some differences in their behaviour. The Mn solution of sample DR07-8 shows enrichment in LREEs (Σ 600 µg/g) compared to the Fe solution (Σ 460 µg/g). MREEs (Σ 22 and 33 µg/g) and HREEs plus Y (Σ 83 and 88 µg/g) have quite similar concentrations in both solutions or a slight enrichment in the iron one (Table 2). Sample DR16-13 has different behaviour, not only in concentration, but also in the mineral phases distribution. The Mn solution preferably concentrates LREEs (Σ 1637 µg/g) twice as much as the Fe solution (Σ 757 µg/g). MREEs are more equally distributed (Σ 59 and 53 µg/g), while the big difference with sample DR07-8 is in the HREEs plus Y, in which the Mn solution (Σ 128 µg/g) is clearly enriched compared to the iron one (80 µg/g).

4.2.3. Electron Probe Micro Analysis (EPMA) and Distribution of Elements

EPMA studies carried out on polished thin sections evidence the differences in mineralogy and microstructures in the two Fe–Mn crusts (Figure 10 and Supplementary Materials Table S1). The occurrence of low backscatter areas corresponding to more porous oxy-hydroxides with mottled to dendritic textures is observed in both samples (Figure 10B,C,H). Spot analysis performed along these low backscatter areas evidences their highest porosity with lower EPMA acquisition, regarding the high backscatter areas. Detrital minerals such as quartz, feldspar or calcite have been identified in low backscatter layers in both crusts. Fe-vernadite, Mn-feroxyhyte, goethite and buserite are identified as Fe–Mn oxyhydroxides (Supplementary Materials Table S2). A great number of foraminifera, showing different substitution degrees by Fe–Mn oxides, are identified in both samples (Figure 10B–D,F).

Crust DR07-8 is mainly composed of stacked lamina forming complex dendritic and columnar growths interrupted by erosive discontinuities or by high-backscatter micro-layers (Figure 10A–D). Colloidal minerals represented by Co-rich Fe-vernadite intergrown with goethite group minerals form the general matrix throughout the crust (Figure 10A–D and Supplementary Materials Table S2). Multiple spot analyses conducted on several laminae show this mineral's textural features and composition (e.g., Figure 10(B-4,C-7,D-9), Supplementary Materials Table S1). The matrix shows similar contents of Mn and Fe (average 20 and 22.6 wt %, respectively), and high contents of Co (0.7 wt %), Ce (0.25 wt %) and V (0.14 wt %). Otherwise, the intercalated bright layers (Figure 10(A-1,C-6)) with thickness of 25–30 µ and more fibrous crystal-textures are composed of 10 Å Mn minerals displaying meaningful higher contents of Mn (average value of 36.7 wt %), Ni (1.2 wt %), Cu (1 wt %) and lower contents of Fe (4.2 wt %), Co (0.33 wt %), and Ce (0.05 wt %) regarding the rest of the growing laminae.

Furthermore, a set of bright laminae growing near erosive discontinuities is formed by goethite and todorokite or busenite caused by the enrichment of Fe or Mn by local re-precipitation (Figure 10(B-3)).

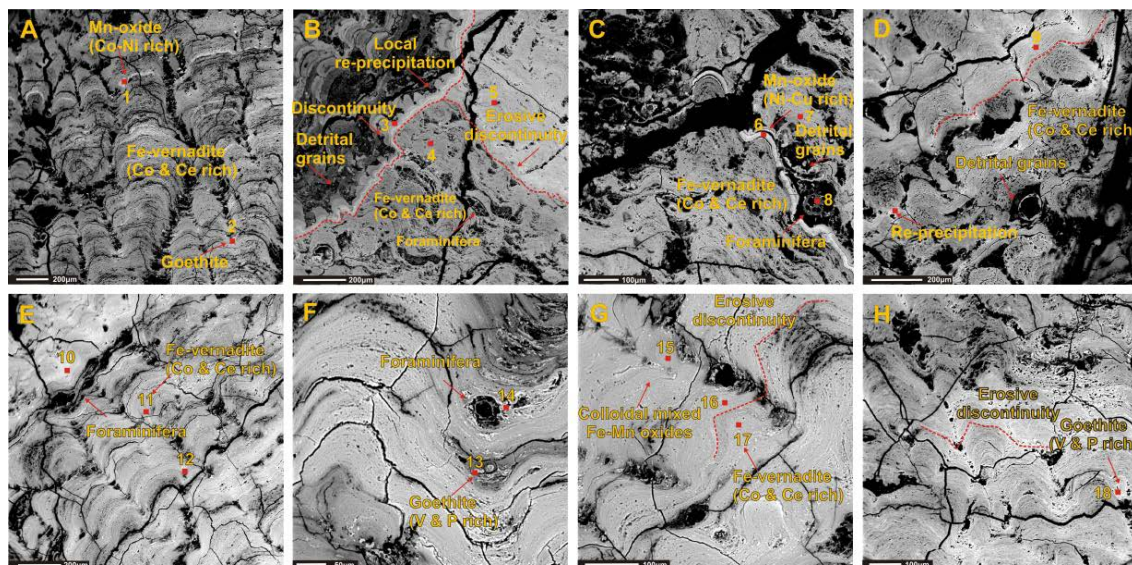


Figure 10. Thin polished-section EPMA photomicrographs (backscatter mode) with the location of microprobe analysis (see Supplementary Table 1), (A–D) Images of DR07-8 and (E–H) of DR16-13. (A) Dendritic branched morphology with thin Co–Ni Mn-oxide laminations (B) Discontinuity with change in accretion direction and erosive parallel discontinuity. (C) Diagenetic Ni–Cu-rich Mn-oxide forming thin lamination. (D) Nodular Fe–Mn re-precipitation and erosive parallel discontinuity. (E) Dense sub-parallel lamination englobing several foraminifera throughout the lamination. (F) Goethite-rich areas, with high contents of V and P, in the convergence of columns. (G,H) Erosive discontinuity clearly recognizable throughout the lamination and goethite-rich aggregates.

Crust DR16-13 shows a more regular growth, consisting of stacked laminae building up large and continuous columns (columnar texture) (Figure 10E–H), that in some areas tend towards dense parallel lamination (Figure 10G). Multiple spot analysis carried out on the stacked laminae identified the next mineral types (Supplementary Materials Table S2): (1) Fe-vernadite with high Mn (23 wt %), Fe (20 wt %), Co (up to 1 wt %), Ce (up to 0.2 wt %) and Ni (up to 0.3 wt %); (2) Goethite, usually at the inflection point of the columns, shows the highest contents of Fe (up to 34 wt %) but the lowest in Mn (4 wt %); (3) Mixed Fe–Mn oxides such as Mn-feroxyhyte. Sometimes, the stacked lamina growth is interrupted by local erosion with subsequent growth (Figure 10G,H). Enriched-foraminifera layers covered by Fe–Mn minerals are also identified on the upper part of columnar growths (Figure 10E,F).

Meaningful mineralogical and geochemical changes are identified along transects carried out from the base to the top of both crusts (Supplementary Materials Table S3). In both crusts, it is possible differentiate chemical changes mainly related to their internal structure. Thus, Layer 4 of crusts shows a dense lamination bounded to a lower growth rate and hydrogenesis. In crust DR07-8, Layer 4 shows higher values for the Mn/Fe ratio (up to 2) and contents of hydrogenetic elements (Mn + Co + Ni + Ce) up to 25 wt %. Similar contents are also found in the dense sub-layer on top of Layers 1, 2 and 3. Otherwise, dendritic to mottled areas show lower contents of these elements (average 20 wt %). On the other hand, dendritic areas are enriched in Fe + V + P (up to 30 wt %) and a consequent Mn/Fe ratio that reaches lower values of 0.5. Otherwise, the identified intercalated bright laminae show a very high Mn/Fe ratio (up to 40) typical of diagenetic growth. Early diagenesis and/or phosphatization in dendritic areas is also responsible for lower Co (down to 0.3 wt %) and Ce (down to 0.1 wt %) contents and relatively high Ni (average 0.5 wt % and locally up to 2 wt %). Crust DR16-13 also shows an increase in the Mn/Fe ratio in Layer 4 up to 1.2, and related Co, Ce and Ni toward the base of the crust

(Mn + Co + Ce + Ni = up to 29 wt %). In this crust, it is also possible to differentiate another increase in the Mn/Fe ratio in the dense sub-layer of Layer 3 that reaches values of 1.6 but a lower percentage of related elements (27 wt %). Through crust DR 16-13, are recognizable several pulses of increase in Mn and related elements (Co, Ni and Ce) in Layers 1 and 2, coinciding with dense sub-layers identified in their uppermost part. In this crust, it is also possible to differentiate that dendritic to mottled areas show higher Fe + V + P contents up to 35 wt %.

4.2.4. Factor Analysis and Mineral Phases

In order to verify the control of the chemical composition between phases, we also conducted a Varimax Q-factor analysis on the results of the EPMA spot analysis. Q-factor returns several important differences between the studied crusts (Table 3).

Table 3. Results of the Varimax factor analysis conducted on the set of EPMA layer-by-layer analyses of both studied crusts. The back color is to differentiate both samples.

	DR07-8					DR16-13			
	Fact. 1	Fact. 2	Fact. 3	Fact. 4	Fact. 5	Fact. 1	Fact. 2	Fact. 3	Fact. 4
Mn		0.87	0.11	0.29	0.14	0.95			0.18
Fe	0.61	−0.34	−0.61	0.19		−0.29	0.88	0.16	
Co	−0.19	0.55	−0.28	0.15	−0.61	0.82	−0.17		
Ni	−0.47	0.62	0.33	0.17	0.17	0.88	−0.24		0.17
Cu	−0.60		−0.16	0.21	0.20	−0.21		0.67	0.14
Ce	0.67	0.37	−0.23	0.29	0.18	0.59	0.58	−0.30	0.21
Mo	0.79	0.27	0.38			0.67	0.12	−0.16	0.14
V	0.75	−0.18	−0.47	0.16	0.14		0.92		0.15
Si		−0.71	0.16	0.56	−0.15	−0.55			0.76
Al	−0.32	−0.22	0.22	0.67		−0.37	−0.46		0.31
K	0.38	−0.37	0.64	0.31	−0.20	−0.30	−0.50		0.72
Ca	0.84	0.27	0.35			0.73		0.21	0.17
Na	−0.44	−0.32	0.31		0.59	0.29	−0.46	0.31	−0.12
Mg	−0.43	0.42		0.35		0.40		0.69	0.18
P	0.88	0.15	0.32			−0.16	0.71	0.53	
Ba	0.28	0.12	−0.45	0.28	0.32	0.24	0.66	−0.53	0.17
W	0.35		0.20	−0.17		0.15		−0.21	

Crust DR07-8 shows five different factors controlling the element composition. Factor 1 controls Fe and several strategic elements such as Ce, Mo, V but also Ca and P. Factor 1 accounts for 29% of the total variance of this sample. It has negative loadings for Ni and Cu. This factor represents hydrogenetically precipitated Fe-oxyhydroxides. Factor 2 controls Mn, Co and Ni and also less Ce and Mo. It has negative loadings for Si, K and Fe. This factor accounts for 17% of the total variance and represents, in general, all the Mn-oxides essentially related to hydrogenesis. Factor 3 controls K, and of minor importance Ca, P, Ni, Mo, Na and Al. It has negative loadings for Fe, V and Ba. This factor likely represents diagenetic minerals (aluminosilicates, Mn-oxides). This factor accounts for 12.3% of the total variance. Factor 4 only accounts for 8.3% of the total variance and controls Si, Al, K and Mg. Factor 4 likely represents detrital input and substrate rock. Factor 5 is only present in crust DR07-8 and it only shows a significant loading for Na and Ba and negative loading for Co. This factor represents 6% of the total variance, representing halite.

In crust DR16-13, only four factors are clearly identifiable. Factor 1 controls the Mn bounded elements Co, Ni, Ce, Mo and also some Ca and Ba. It has negative loadings for Si, Al and K. Factor 2 is essentially related to Fe bounded elements that are V, P, but also part of the Ce and Ba. It has negative loadings for Al, K and Na. These two factors represent essentially Fe and Mn hydrogenetic precipitation and account for 29 and 21% of the total variance, respectively. Factor 3 controls Cu with Ca, Mg and P. It has negative loadings for Ce and Ba. This factor mostly represents the presence of

CFA and bioclast input and accounts for 10% of the total variance. Finally, Factor 4 controls Si, K and Al due essentially to detrital input, accounting for 9.2% of the total variance.

4.2.5. Growth Rate and “Cobalt Chronometer” Age

Growth rates have been calculated using the “cobalt chronometer” [62]. The calculated growth rates, carried out on bulk samples of both crusts, yield similar growth rates of 1.9 and 1.8 mm/Ma for crust DR07-8 and DR16-13, respectively (Figure 11). Based on these growth rates, the ages calculated for the initiation of Fe–Mn crust growth are 32 and 50 Ma, respectively. These ages are based on bulk values and consider the average thickness of the whole crust. However, these values do not consider variation in changes in accretion over time, and the occurrence of erosional or hiatus events.

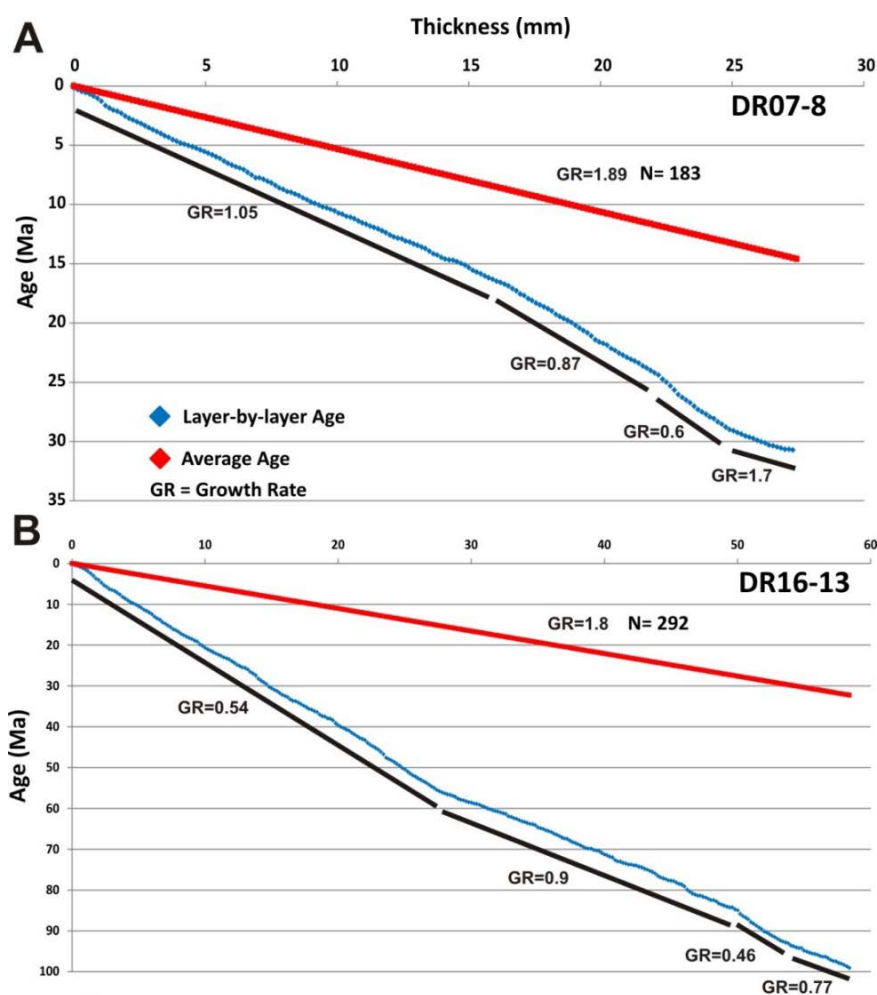


Figure 11. Layer-by-layer growth rate and age compared with bulk average growth rate and age of (A) crust DR07-8 and (B) crust DR16-13. Both crusts show several sections with different mean growth rates identified by black continuous lines.

In this way, to calculate high-resolution growth rates, two transects of 183 and 292 layer-by-layer EPMA analysis have been carried out along the growth axis of both crusts. Based on these transects, mean growth rates yield values of 1.02 and 0.82 mm/Ma for crust DR07-8 and DR16-13, respectively. The growth rates are different to those calculated based on bulk chemistry due to a better resolution of the layer-by-layer technique. Based on these high-resolution growth rates, the ages of 30 Ma (early Oligocene) and 99 Ma (Cenomanian, early Upper Cretaceous) have been determined for DR07-8 and DR16-13 crusts, respectively (Figure 11).

Crust DR07-8 shows a similar age to that calculated based on bulk analysis, which indicates constant growth (Figure 11A). By contrast, crust DR16-13 shows an almost twice as old age, indicating that bulk analysis does not consider increasing or decreasing rates of growth evidenced by the layer-by-layer analysis (Figure 11B).

The high-resolution analyses show diverse episodes characterised by different accretion growth in both crusts (Figure 11). Crust DR07-8 shows four different periods of growth rates: (a) a first period, from the substrate rock to ca. 28.7 Ma (early-late Oligocene) characterised by high growth rates (mean 1.7 mm/Ma with maximum of 20 mm/Ma); (b) a second period from 28.7 to 24.5 Ma (late Oligocene-earliest Miocene) with low growth rates of 0.6 mm/Ma; (c) a third period, from 24.5 to 14.5 Ma (early to middle Miocene) characterised by an increasing growth rate up to 0.87 mm/Ma; and (d) a fourth period, from 14.5 Ma (Middle Miocene to Present) to the top of the crust, displaying higher growth rates of 1.05 mm/Ma (Figure 11A). Crust DR16-13 also shows four periods of growth rates. Period 1 (99 to 92 Ma, Cenomanian-Turonian, early Upper Cretaceous) and 3 (84 to 58 Ma, late Upper Cretaceous to late Paleocene) exhibit similar high growth rates of 0.77 and 0.9 mm/Ma, respectively. Additionally, periods 2 (92 to 84 Ma, Turonian to Campanian, late Upper Cretaceous) and 4 (58 Ma to the top, Eocene to Present) show lower growth rates of 0.46 and 0.54 mm/Ma, respectively (Figure 11B).

5. Discussion

The ferromanganese crusts from The Paps and Tropic seamounts reveal a complex mineralogy and geochemistry due to their long history of mineral growth since 30 Ma (early Oligocene) and 99 Ma (Upper Cretaceous) ago, respectively. The petrographic, mineralogical and geochemical high-resolution analyses allow the differentiation of hydrogenetic and diagenetic processes involved in the growing history of the crusts. Moreover, enrichments in critical minerals seem to be controlled by different oceanographic and geological factors at different scales, i.e., global, regional and local. Therefore, in this section, we address three main issues derived from the high-resolution analyses of the crusts: (i) the type of processes contributing to the growth of the crusts; (ii) the main mineralogical changes, and (iii) the factors involved in the enrichments in critical elements.

5.1. Genesis of Fe–Mn Crusts Based on High-Resolution Analyses

Bulk mineralogical and geochemical studies carried out previously on the CISP crusts revealed that ferromanganese crusts were formed mainly by hydrogenetic processes [27]. The mineralogy of the crusts is composed essentially by Fe-vernadite (more than 90%) and goethite group minerals. This mineralogy reflects the predominance of the hydrogenetic process during their formation, similar to ferromanganese crusts from the Atlantic, Pacific and Indian oceans (e.g., [8,69–71]). In addition, bulk geochemistry also supports the hydrogenetic origin of the crusts. The Mn/Fe ratio (1.03 and 0.78) for both crusts falls within the average values for hydrogenetic crusts from the Atlantic Ocean (means of 0.8) but slightly lower than the ratio for Pacific crusts (mean of 1.4) [6,15,70]. Moreover, the bulk values plotted on the Mn–Fe–(Co + Ni + Cu) \times 10 ternary diagram (Figure 12A,B) modified from [16,72,73] and REYs average values of 2400 μ g/g are in the mean for hydrogenetic growth, and the plot of indexes obtained ([11,70], Figure 12C,D modified from [74]) also falls within the hydrogenetic field.

However, high-resolution EPMA analyses allow the recognition of micro-laminations associated with different genetic processes. These high-resolution data plotted on the Mn–Fe–(Co + Ni + Cu) \times 10 ternary diagram show a bigger dispersion of genetic processes than previously observed by bulk analyses (Figure 12A). In this way, the high-resolution analyses of microlayers of crust DR07-8 fall within the diagenetic or mixed hydrogenetic/diagenetic fields (Figure 12A). Furthermore, high-resolution analyses evidence mineralogical and geochemical differences between the two crusts related to their growth history. Petrographic and XRD analyses show that in crust DR07-8, the abundance of detrital and authigenic minerals is higher than in crust DR16-13 (Table 1 and Figure 5). The major detrital input in crust DR07-8 is also associated with higher alumina-silicates (Si + Al + K +

Ca + Mg), reaching contents of 21.3 wt % in contrast to the values of 6.3 wt % found in crust DR16-13 (Table 2). The occurrence of alumina-silicate detrital grains in crust DR07-8 is also evidenced by EPMA analysis and SEM microphotography (Figure 6C,E and Figure 10A,B,D). Additionally, the growth of authigenic CFA related to pervasive phosphatization of crust DR07-8 is evidenced by their higher contents of P_2O_5 (3.7 wt %) and CaO (8.2 wt %) (Figure 4), and this is reflected in XRD experiments (Figure 5A) and petrographic observations. Phosphatization in this ferromanganese crust occurs by means of preferential replacement of carbonates and Fe-oxyhydroxide (e.g., [75–79]). This process can strongly modify the crust mineralogy by increasing their Mn/Fe ratio [10,79], as observed in DR07-8 crust reaching Mn/Fe ratios up to 1.03. The presence of biological input in the CISP Fe–Mn crusts was already evidenced in previous studies in the Macaronesia region (e.g., [27,80]). High-resolution analyses also evidence abundant coccoliths and the dispersal of filament structures related to the microbial activity (Figure 6E), similar to those described in other Fe–Mn crusts and nodules [81–83].

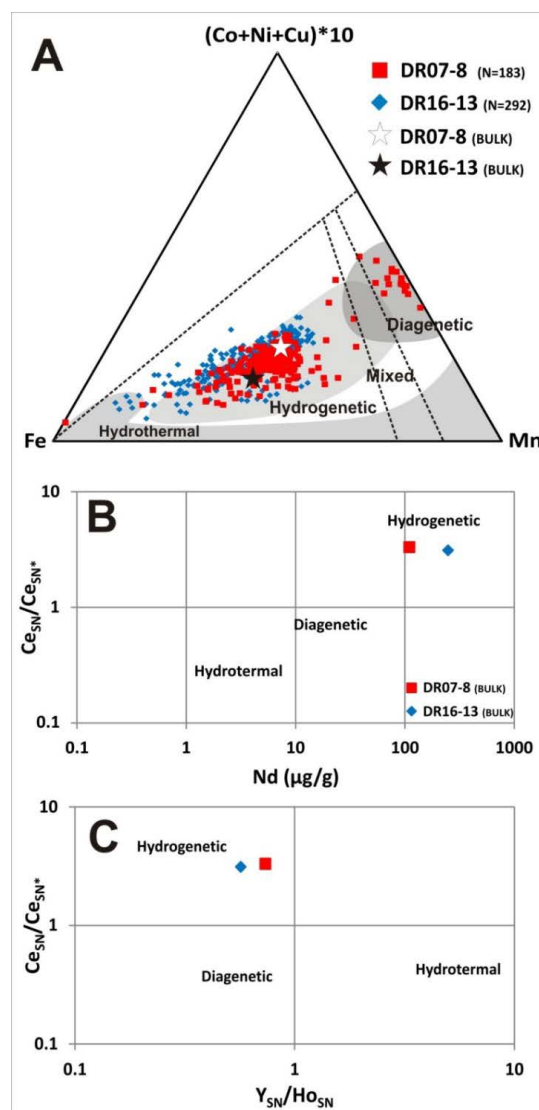


Figure 12. (A) Ternary diagram modified from [18,72,73]. Bulk analysis is represented by stars plotted in the hydrogenetic field and compared with hundreds of EPMA spot analyses that are plotted in the diagenetic field; (B,C) Binary diagrams of bulk REYs data (after [74]) are also plotted in the hydrogenetic field.

High-resolution analyses of both crusts show that layers and sub-layers show a rhythmic behavior. In this way, we suggest that the alternation between dense lamination packages and more dendritic mottled growth patterns might be related to (i) changes in the regional oceanographic setting, such as the thickness of the OMZ, and/or (ii) the influence of different growth mechanisms other than purely hydrogenetic (Figures 3, 4 and 10). Thus, dendritic patterns are associated with high growth rates (up to 4 mm/Ma) affected by a narrower OMZ, whereas the dense parallel growth is related to low growth rates (down to 0.5 mm/Ma), bathed by a thick OMZ (e.g., [14,84–86]). EPMA analyses of DR07-8 crusts show a typical botryoidal morphology (Figure 10A), interpreted as a response to pulses of high growth rates. Otherwise, DR16-13 crusts show thick sub-parallel layers and sub-layers (Figure 10E), typical of low accretion rates due to chemical precipitation of Fe–Mn colloids from cold seawater by hydrogenesis (e.g., [6,15,84–86]).

Crust DR07-8 shows bright intercalated microlayers formed by a 10 Å mineral (Figures 5A and 10A,B; Supplementary Materials Tables S1 and S2) enriched in Mn (up to 40 wt %), Ni (up to 2 wt %) and Cu (up to 1 wt %), but with low contents of Fe (2.5 wt %), Co (0.3 wt %) and Ce (0.04 wt %). Similar metallic contents have been reported in abyssal diagenetic nodules [6,8,10,15–18]. According to our thermic, CEE experiments and geochemical studies, this mineral would represent a diagenetic Mn mineral, probably an intergrowth between buserite and asbolane. Buserite might change its structure to todorokite if conditions are favorable (e.g., [10,17,61,87–91]). We suggest that the formation of these bright Fe–Mn interlayered laminations might be formed during periods of increasing input of sediments driven by undercurrents that temporally covered the crust, promoting oxic/sub-oxic diagenetic accretion. This hypothesis is supported by the presence of erosive discontinuities and detrital alumina-silicate grains overlying these diagenetic bright laminations and reflecting an increase in undercurrent strength (Figure 10A–D).

Additionally, crust DR16-13 exhibits only hydrogenetic minerals, showing contents of Mn (up to 18 wt %) and Fe (up to 25 wt %), coherent with the presence of Fe-vernadite intermixed with goethite. EPMA high-resolution analysis shows in this crust a certain linear trend of values towards the hydrothermal field (Figure 12A). We interpret this trend as an artifact due to areas strongly enriched in goethite within the laminations (Figure 10F,H and Supplementary Materials Tables S1 and S2). Furthermore, bright laminations evidencing diagenetic processes are not identified in this crust DR16-13. In this way, the contents of Fe and Mn are constant, ranging between 22 and 35 wt % and 14 and 30 wt %, respectively. These values fit with those average values reported for purely hydrogenetic crusts in the Atlantic Ocean (e.g., [5,6,11,15,70,71,92,93]).

Bulk geochemistry also reveals differences in contents of trace elements between the two crusts. High contents of Co, Ce and Mo elements are related to hydrogenesis. Co and Ce are elements that are concentrated in Fe–Mn crusts by direct oxidation of Co^{4+} and Ce^{3+} from seawater incorporated into freshly precipitated oxides [2,4–6,8,12,15,24,25,94]. Crust DR16-13 shows higher contents of Co, Ce and Mo (5500, 2000 and 700 µg/g, respectively) than crust DR07-8 (3200, 900 and 270 µg/g, respectively). The highest contents of Co and Ce observed in crust DR16-13 (up to 1.5 and 0.32 wt %, respectively) are consistent with a low-growth rate period identified in the EPMA transect (mean GR = 0.8 mm/Ma). In contrast, crust DR07-8 shows the lowest contents of both elements related to periods of high-rate growth up to 2 mm/Ma. The concentration of Co, Ce and Mo related to hydrogenetic Fe–Mn oxides formation is also confirmed by the factor analysis. Thus, on both crusts, it is possible to determine that the source of these elements is strictly associated with the presence of Fe and Mn (Factor 2 DR07-8 and Factor 1 DR16-13, Table 3).

Crust DR07-8 shows high contents of Ni and Cu (4800 and 1300 µg/g, respectively), similar to those reported in Pacific crusts. In contrast, crust DR16-13 shows lower contents of Ni and Cu (3200 and 700 µg/g, respectively), more similar to those reported in the Atlantic Ocean crusts (Table 2) (e.g., [6,8,11,12,15–17,70,71,94]). EPMA analysis evidences that the higher contents of Ni and Cu are associated with Mn-rich minerals (with Mn/Fe ratios up to 40) as diagenetic buserite/asbolane, which form thin bright interlayered laminations (Supplementary Materials Tables S1–S3). The source of Ni

and Cu associated with Mn minerals is also recognizable in factor analysis of DR07-8 crusts [95,96] (Factors 2 and 3 DR07-8 Table 3). It is worth noting that Ba is another interesting element. In this way, the contents of Ba are strictly related to the presence of Fe-vernadite, and are a consequence of hydrogenesis processes. However, a biogenic input during the crusts' growth is also derived from the factor analysis [6,12,79] (Table 3). In this way, crust DR16-13 shows higher contents of Ba (2000 µg/g) than crust DR07-8 (1067 µg/g) and positive correlation both with the Mn and Fe hydrogenetic phases. Ba input to the oxides was supported by dissolution of algae and/or plankton and foraminifera in the water column during periods of high bioproductivity (e.g., [6,15]).

The abundance of REY elements is also associated with low-growth rate periods during the hydrogenetic formation of the crusts [4,94,97,98]. This relationship has also been evidenced in the CISP crusts [27]. Crust DR16-13 shows higher REYs contents (3000 µg/g) than the sample DR07-8 (1400 µg/g). These higher contents are essentially due to higher LREE contents of DR16-13 (2742 µg/g) than in DR07-8 (1238 µg/g), and also to the MREE contents (132 versus 67 µg/g, respectively). However, the contents of HREEs (287 and 307 µg/g, respectively) show quite similar values in both crusts with a slight enrichment in crust DR07-8. Crust DR07-8 shows a meaningful enrichment in Yttrium (225 µg/g) due to the presence of layers enriched in CFA and pervasive phosphatization. Yttrium is interpreted as being sourced from the phosphate deposits located in the Western Sahara and incorporated into the crusts by Saharan dust input [6,8,9,27,99]. EPMA spot analysis shows that the Ce contents in hydrogenetic minerals (Fe-vernadite) of both crusts are almost constant (~0.2 wt %), but lower in the goethite-enriched layers (0.1 wt %), decreasing considerably in diagenetic Mn-rich minerals such as busserite, (down to 0.05 wt %).

5.2. Association of Metals with Different Mineral Phases

Sequential leaching experiments carried out on both crusts show how strategic and critical metals are associated with different minerals.

5.2.1. Major Elements Defining the Main Mineral Phases

Selective leaching of elements associated with the main four fractions, i.e., carbonate, Mn-oxides, Fe oxyhydroxides, and residual minerals evidence the behavior of the critical elements of the ferromanganese crusts.

Leaching of carbonates dissolves practically the totality of Ca, Na, Mg and S. These elements are essentially associated with the occurrence of calcite and dolomite. S can also be associated with carbonates as minor element. Most of Ca and Mg are contained in the bioclasts (coccoliths and foraminifera) and detrital grains sourced from the Saharan dust, as occurs in other crusts from the Macaronesia (e.g., [11,27,100]). Additionally, the Ca contents of crust DR07-8 affected by phosphatization also form part of CFA.

Leaching of Mn-oxides concentrates up to 100% of the manganese, and part of the total Fe content (1.33 and 1.79 wt %, respectively) (Table 2). The Fe incorporation identified in this step is consistent with the presence of Fe-vernadite [2,5–8,15,23,69,80,101]. Beside the concentration of major elements, crust DR07-8 concentrates more Mg than DR16-13 (0.27 vs. 0.07 wt %, respectively). This difference is related to the occurrence of diagenetic Mn-minerals such as the busserite or birnessite forming bright laminae as observed in sample DR07-8 (e.g., Figure 10A). Electron Probe analyses show that these laminations concentrate up to three times the contents of Mg than the other hydrogenetic laminae. This enrichment in Mg is provided by the large spacing of these minerals (10 Å), without cation exchange power (Figure 5C), allowing the entrance of more Mg^{2+} ions within their structure with respect to δ -MnO₂ [87,91,101].

Leaching of Fe oxyhydroxides concentrates essentially the Fe with minor amounts of Mn (0.34 and 0.48 wt %, respectively), probably forming part of Mn-bearing FeOOH (Mn-feroxyhyte) [6,15,102]. This fraction also concentrates significant amounts of Al (1.14 and 0.33 wt %), Ti (0.44 and 0.32 wt %), and P (0.4 and 0.2 wt %). The concentration of these elements is associated with the presence of iron detrital

minerals or generated by an early phosphatization event in DR07-8 crust (e.g., [75–79]). Detrital or volcanoclastic minerals represented by minor contents of titanomagnetite, pyroxene or amphibole, and authigenic CFA partially dissolved in this leaching step are commonly associated with the presence of Fe [6,15,69].

Finally, leaching of residuals concentrates the rest of the aluminum silicate elements. In this fraction, quartz and feldspar are essentially dissolved. In crust DR07-8, the enrichment in detrital minerals is evident with respect to DR 16-13 for the highest contents of Al (0.83 vs. 0.28 wt %), K (0.23 vs. 0.10 wt %) and Na (0.13 vs. 0.01 wt %).

5.2.2. Manganese Oxides as Critical Minerals with High Contents of Co, Ni and Cu

The trace elements speciation in the four extracted steps shows significant differences between the crusts. In step 1, bounded by carbonates and sulphates, minor amounts of trace elements are concentrated. These trace elements consist of Ni (225 and 151 µg/g, respectively), Cu (73 and 23 µg/g), and Zn (59 and 44 µg/g) related to biological inputs such as foraminifera and coccoliths (Figures 6 and 10), reported in other areas ([103,104] and references therein) and bounded to carbonates and phosphates (e.g., [15,44,69,100]).

Regarding the contents in seawater, Co, Ni, Cu and other elements (i.e., Bi, Te, Pb) are strongly enriched, between 10^8 to 10^{10} times, in the ferromanganese crusts and nodules [2,6,8,10,15]. These elements are strongly concentrated in the Mn-oxides and Fe-oxyhydroxides leached in steps 2 and 3. The leaching of these two main fractions helps to distinguish between genetic processes affecting the growth of the crust. The concentration of Co and Ni elements seems to be strictly related to manganese oxides as observed in Table 2 and reported in other works (e.g., [3,6,15,44,69,76,105]). In this way, the Mn oxides fraction of the mixed hydrogenetic/diagenetic crust DR07-8 concentrates lower Co (3000 µg/g) but higher Ni (4200 µg/g) than the purely hydrogenetic crust DR16-13 (5200 and 2500 µg/g, respectively). The concentration of Cu also shows some differences between the crusts. The mixed hydrogenetic/diagenetic crust DR07-8 shows a concentration in Cu mainly linked to the Mn phase (L2 = 680 µg/g, L3 = 410 µg/g), whereas in the purely hydrogenetic crust DR16-13, the Cu contents are mostly concentrated in the Fe phase (L2 = 200 µg/g, L3 = 430 µg/g).

The differences in the Co, Ni and Cu contents between the two types of crusts seems to be related to the type of minerals associated with the genetic processes as discussed above. The mixed hydrogenetic/diagenetic crust DR07-8 presents two types of manganese oxides: (i) the hydrogenetic Fe-vernadite, as the main Mn oxide within the crust, and (ii) the diagenetic busserite/asbolane. The Fe-vernadite concentrates essentially Co and Ni [2,6,8,15,23–25,44,69]. Consequently, EPMA spot analyses of the Fe-vernadite show high concentrations of Co (7000 µg/g) and Ni (3000 µg/g), but lower contents of Cu, (500 µg/g) (Supplementary Materials Tables S1 and S2). Additionally, busserite/asbolane concentrates very high contents of Ni (up to 2.3 wt %) and Cu (up to 1.5 wt %) but lower contents of Co (up to 4000 µg/g with mean contents of 2000 µg/g). Similar contents of Ni, Cu and Co have been found in diagenetic nodules of the Clarion Clipperton Zone (CCZ) (e.g., [6,8,10,16,18,77,87,95,96,106]). For this reason, the Mn oxide fraction of mixed hydrogenetic/diagenetic crust DR07-8 shows higher values in Ni and Cu in comparison with the purely hydrogenetic crust DR16-13 bearing common contents of Cu linked to Fe as reported in similar hydrogenetic crusts (e.g., [6,12,44,107]).

Leaching of Mn oxides also concentrates other critical and strategic elements with respect to Fe-oxyhydroxides. Therefore, elements such as V (400 and 600 µg/g), Zn (260 and 270 µg/g) and Ti (82 and 106 µg/g) are concentrated in the crusts DR07-8 and DR16-13, respectively. A minor part of these elements is also concentrated in the Fe-oxyhydroxides step (see the Fe-ox column for these elements in Table 2) as reported in previous works (e.g., [6,8,10,12,15,44,79,108]).

The leaching step 3 (Fe-oxyhydroxides) also shows differences in element concentrations between the two types of crusts. The most evident difference is shown in the Pb contents, an element related to Fe-oxyhydroxides by hydrogenetic formation of crusts (e.g., [2,6,8,15,24]). Therefore, the Pb content of the purely hydrogenetic crust DR16-13 (1500 $\mu\text{g/g}$) is clearly higher than that of the mixed diagenetic/hydrogenetic crust DR07-8 (1000 $\mu\text{g/g}$). Additionally, the contents of As (400 and 280 $\mu\text{g/g}$, respectively) are higher in purely hydrogenetic crusts, being related to the biological activity and/or hydrogenetic precipitation of Fe hydroxides. Other elements such as Be, Sb, Nb, Se, Th and U are also enriched in the Fe-oxyhydroxides step. In seawater, these elements usually form big and generally poorly negatively charged anions that bind with the poorly positively charged Fe-oxyhydroxides [6,8,16,69,79,107].

Furthermore, Mo is another strategic metal appearing enriched in Fe–Mn crusts by almost two orders of magnitude with respect to the average composition of the continental crust (Figure 8). Thus, Mo is almost entirely concentrated in the Fe-oxyhydroxides fraction in crusts DR07-8 and DR16-13 (240 and 570 $\mu\text{g/g}$, respectively), as also reported previously in other areas (e.g., [12,44]). This behavior is consistent with earlier studies that consider Mo as a negatively charged ion dissolved in seawater [2,6,15,24]. Moreover, detailed synchrotron analysis showed that Mo is definitely bounded to the Mn octahedra and not to Fe [107,109,110]. Based on these results, we suggest that the presence of Mo in the iron phase is an artifact or can probably be caused by (i) an early re-precipitation, and (ii) an increase of insolubility of Mo during the hydroxylamine leaching of the Mn oxides, that later is dissolved with Fe in a more reactive hydrochloride acid leaching.

5.2.3. REYs Scavenging between Fe and Mn Phases as Record of Different Genetic Processes

The distribution of REE contents after leaching Mn-oxides and Fe-oxyhydroxides shows some meaningful differences (Table 2). In both crust types, Ce is the most abundant REE in the bulk sample, and it shows higher scavenging in the Mn-oxide phase (460 and 1250 $\mu\text{g/g}$, respectively, vs. 360 and 580 $\mu\text{g/g}$ for the Fe-oxyhydroxides). The enrichment of Ce in Mn-oxides is explained by Ce (III) oxidation to Ce (IV) by biological reactions or surface-catalysis and typical of hydrogenesis (e.g., [6,15,97,111,112] and references therein).

Furthermore, the contents of La and Pr show similar behavior. La is also enriched in the Mn-oxide phase (83 and 215 $\mu\text{g/g}$ for crusts DR07-8 and DR16-13, respectively) with respect to the Fe-oxyhydroxide phase (34 and 50 $\mu\text{g/g}$). In the mixed diagenetic/hydrogenetic crust DR07-8, the enrichment in REE during the Mn-oxide leaching affects only the La and Ce elements. In contrast, the purely hydrogenetic crust DR16-13 appears enriched in other REE elements such as Pr and Nd (37 and 140 $\mu\text{g/g}$, respectively) in the Mn-oxide phase with respect to the Fe-oxyhydroxide phase (23 and 100 $\mu\text{g/g}$, respectively).

MREEs and HREEs show distinct behaviors depending on the type of genetic model. The mixed diagenetic/hydrogenetic crust DR07-8 appears slightly enriched in HREEs during the Fe-oxyhydroxides leaching. This fact is explained by previous experiments showing that Gd and Yb at a normal seawater pH are slightly more enriched in Fe-oxyhydroxides than in Mn-oxides [111]. In this way, the evidence of the enrichment in HREEs related to Fe-oxyhydroxides is confirmed in the two types of crusts (Table 2). Nevertheless, the high contents of phyllo-manganates contained in the purely hydrogenetic crust DR16-13 partially mask this behavior. The enrichment in HREEs observed in the mixed diagenetic/hydrogenetic crust DR07-8 is clearly related to the Fe-hydroxides.

The scavenging of REYs between Mn-oxides and Fe-oxyhydroxides is still under discussion. Previous studies report that the difference in scavenging of REYs between the iron and manganese phases depends on several factors: (i) the oxidation state of the element; (ii) the solubility of the dissolved ions; (iii) the pH of local waters; and (iii) the charge of the oxides surface (e.g., [97,111,112]). Based on the study of purely hydrogenetic Fe–Mn crusts from the Pacific Ocean, some authors support that the scavenging of REYs between Mn-oxides and Fe-oxyhydroxide is not clear [94,107,113].

In order to compare the behavior of REY with respect to Mn- and Fe-oxyhydroxides in our crusts with those Fe–Mn crusts reported by [94], we plot the contents of REYs for each of the four leaching fractions normalised to PAAS (Figure 13A) and data from these authors (Figure 13B). In Figure 13A, the four leaching steps (carbonates, Mn-oxides, Fe-oxyhydroxides and residuals) are plotted for both types of genetic crusts (mixed diagenetic/hydrogenetic DR07-8 crust as red lines, and purely hydrogenetic DR16-13 crust as blue lines).

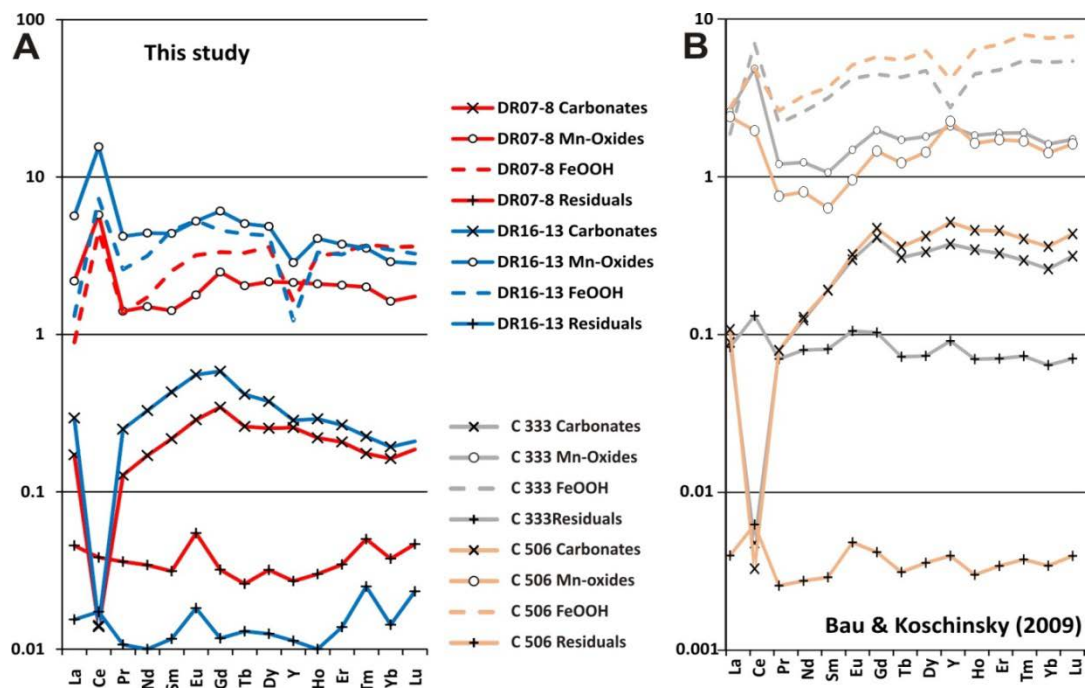


Figure 13. The four sequential leaching fractions corresponding to carbonates, Mn-oxides, Fe-oxyhydroxides and residuals obtained in both crusts normalised to PAAS [68]. Comparison ratio between (A) the leaching fraction of this study's crust and [94] (B).

CISP crusts show a gradual enrichment of MREEs and HREEs in the Fe-oxyhydroxide phase with respect to the Mn-oxide phase. The behavior of Mn-oxide and Fe-oxyhydroxide phases in the CIPS shows some differences to those reported by [94]. These authors conducted a similar sequential leaching experiment with two Fe–Mn crusts from the Central Pacific. CISP crusts show the occurrence of a clear Ce positive anomaly both on the Mn-oxide and Fe-oxyhydroxide leaching steps. This anomaly is especially relevant for the Mn-oxide phase (Figure 13A). In contrast, data from [94] show this positive anomaly in Ce higher in the Fe-oxyhydroxide phase (Figure 13B). Furthermore, the negative anomaly in Y depicted for the Fe-oxyhydroxide phase by [94] is also shown in the CISP crusts. A similar negative anomaly is found in the Mn-oxide phase of the hydrogenetic crust DR16-13 but not for the corresponding phase in the mixed diagenetic/hydrogenetic DR07-08 that shows a behavior similar to [94] samples (Figure 13). For the carbonates and residual fractions, the REYs show very low contents in both crusts in agreement with data from [94].

The mixed diagenetic/hydrogenetic crust DR07-8 displays similar REY contents to one of the samples reported by [94], averaging 1600 and 1519 $\mu\text{g/g}$, respectively. This mixed crust DR07-8 shows lower concentrations of REYs in the Mn-oxide phase. This is consistent with data from EPMA spot analysis. Thus, Mn-rich bright laminations identified in this crust with a clear diagenetic origin, and growth rates of up 6 mm/Ma yielded very low contents of Ce (0.05 wt %). We suggest that the influence of these diagenetic laminations on the overall geochemistry of the Mn-oxides fraction might explain the low REY contents in this phase.

On the other hand, the purely hydrogenetic crust DR16-13 shows a strong difference in the REY patterns from those reported by [94], and behavior and contents quite similar to those from the [111] experiment with major concentrations of LREEs and MREEs in the Mn-oxide phase. Therefore, enrichment of REYs in the Mn-oxide phase is clearly evidenced for this pure hydrogenetic crust DR16-13. However, Yb and Lu appear enriched only in the Fe-oxyhydroxide phase (Figure 13A).

5.3. Composition Changes along the Growing History of the Crusts

EPMA layer-by-layer transects evidence the different behavior of the strategic elements since the onset of mineral growth. An interpretative cartoon model for crust growth is presented in Figure 14. In both crusts, a clear decrease in the Mn/Fe ratios of at least 30 Ma is evidenced to the present time. This is also linked to the enrichment in Co, Ce and Ni contents, particularly between 22 and 29 Ma (Supplementary Materials Table S3). These enrichments in Mn, Co, Ce and Ni at about the same age range have already been observed in other ferromanganese crusts from the CISP [27], associated with the spreading of the Oxygen Minimum Zone (OMZ) during this period. Thus, the increase of the OMZ thickness induces slower growth rates (0.6 and 0.46 mm/Ma for DR07-8 and DR16-13, respectively), promoting the enrichment of metals within the Mn-Fe oxyhydroxide structures [6]. In crust DR16-13, another event of enrichment in Mn, Co, Ce and Ni contents takes place from 84 to 92 Ma, also being associated with the extent of the OMZ (Supplementary Materials Table S3). Furthermore, we suggest that these slow growth rate events are responsible for the formation of the thin dense-subparallel lamination patterns identified within the sub-layers of both crusts (Figure 3) in periods with very low input of bottom undercurrents and no upwelling phenomenon (Figure 14A). On the other hand, the rest of the growth period of both crusts shows enrichment in Fe and P but also in detrital and bioclast inputs. This is linked to dendritic to mottled areas that show a higher growth rate (average 2 mm/Ma with higher values up to 6 mm/Ma). The increase in the growth rate depends on a narrowed OMZ that promotes a higher precipitation of the Fe-Mn oxyhydroxides. Thus, a higher growth rate and related structure is also due to an increase of currents action and/or fertilization of the Atlantic Ocean in the CISP area (Figure 14B). Currents move nutrients from the deep ocean, promoting an intense bioproductivity that is also favored by the contribution of the Saharan dust [27]. This is supported by the presence of several foraminifera and coccolithos found in these layers (Figure 10B,C,E,H). In the same mottled to dendritic layers, an increase of the detrital input is also evident due to both the action of the currents and from Saharan wind inputs (Figure 10B–D). In addition, early diagenetic micro-layers, very enriched in Cu and Ni, have been observed in the mottled to dendritic layers.

Layer-by-layer analyses (Supplementary Materials Table S3) also evidence an increase trend in the contents of Fe and V during the last 30 Ma in both crusts, consistent with previous studies on Fe-Mn crusts (e.g., [6,15,69]). The increase of Fe and P since the early Miocene, identified in both crusts, is associated with the formation of the Saharan desert and the increase of dust input in the Atlantic Ocean [27]. In crust DR16-13, three other periods with enrichments in Fe and V are identified at 30–65, 67–73, and 75–94 Ma. On the other hand, the abrupt increase in the Fe contents identified between 70 and 80 Ma within crust DR16-13 might be related to the massive Fe input into seawater, caused by the last submarine eruptions that occurred within the CISP region [39].

Finally, the occurrence of pervasive phosphatization and Fe-Mn re-nucleation, especially recognizable in the middle part of crust DR07-8, rich in carbonate bioclasts, is linked to global phosphogenetic events that occurred in the Early Miocene between 24 and 17 Ma (e.g., [14,27,76]).

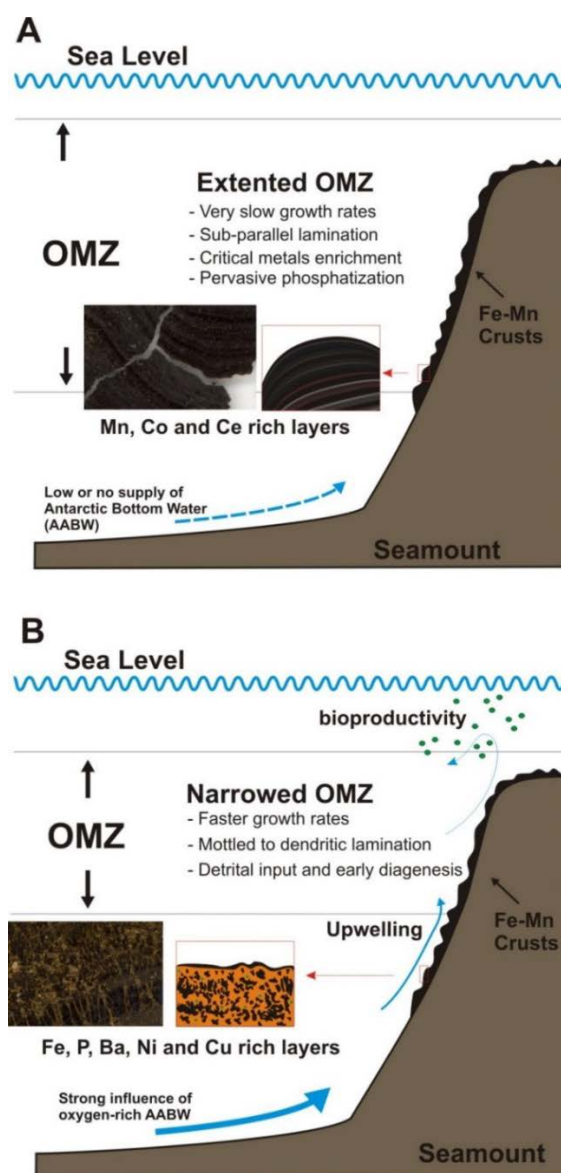


Figure 14. Model of the formation of Fe–Mn crusts in the CISP with textural features and metal enrichment characteristics. **(A)** periods of extended OMZ lead to the formation of sub-parallel lamination with low growth rates. **(B)** periods of narrowed OMZ lead to the formation of dendritic to mottled laminations with high growth rates. See the text for further explanation.

6. Conclusions

Two Fe–Mn crusts among 35 samples, from six seamounts in the CISP, were selected as representatives of the endpoint members of two distinct types of genetic processes, i.e., mixed diagenetic/hydrogenetic and purely hydrogenetic. In this way, high-resolution analyses (petrographic microscopy, XRD, SEM, HR-TEM, EPMA) together with thermic treatment, cation exchange, leaching experiments and chemical determinations have pursued the main aim of distinguishing the critical elements, and their association with mineral phases and genetic processes forming long-lived Fe–Mn crust. The main outcomes of this work can be summarised as follows:

- (1) The Fe–Mn crust (DR16-13) collected on the eastern side of the Tropic Seamount has a mean thickness of 9 cm, showing no botryoids on its surface, mainly composed of dense laminations of Fe-vernadite (more than 90%) and goethite group minerals. This mineralogy

reflects the predominance of the hydrogenetic process during their formation, similar to other ferromanganese crusts from the Atlantic, Pacific and Indian oceans [2,4,6,15,23,44,63,92,93]. Based on the high-resolution “cobalt chronometer” age calculation, this purely hydrogenetic crust yielded an age of 99 Ma (Upper Cretaceous). The onset of crust growth is consistent with the age of the volcanic formation of the Tropic Seamount dated at 119 Ma [39]. This means that this crust would be one of the oldest Fe–Mn crusts of the Atlantic Ocean.

- (2) The Fe–Mn crust (DR07-8), collected in the western side of The Paps Seamount, has a maximum thickness of up to 8 cm, showing typical botryoids on its surface reaching diameters of 1–2 cm. Based on the “cobalt chronometer” for age calculation, this crust began to grow 30 Ma ago (early Oligocene). More than 240 EPMA spot analyses of the microlayers indicate a hydrogenetic or mixed hydrogenetic/diagenetic origin. High-resolution mineralogical analyses show two main types of manganese oxides: (i) hydrogenetic Fe-vernadite, as the main Mn oxide, and (ii) a 10 Å phyllomanganate interpreted as an intergrowth of buserite and asbolane. Bright laminae of diagenetic buserite/asbolane appear on overlying dendritic growths of hydrogenetic Fe-vernadite. Additionally, the occurrence of authigenic calcite, palygorskite and carbonate fluor-apatite (CFA) suggests early diagenesis and pervasive phosphatization events.
- (3) Sequential leaching analysis indicated that Co, Ni, Cu, Ba and Ce are linked to Mn minerals. Therefore, Mn-oxides are enriched in Ni and Cu by diagenetic processes or in Co and Ce by hydrogenetic processes. On the other hand, Fe-oxyhydroxides concentrate V, Zn, As and Pb. The distribution of REYs depends on the type of genetic processes. Thus, mixed diagenetic/hydrogenetic crusts show enrichment in MREEs and HREEs in the Fe-oxyhydroxide phases, whereas the purely hydrogenetic crust shows a slight enrichment of all REY (and especially LREE) elements in the Mn-oxide phases.
- (4) Differences in the Co, Ni and Cu contents between the two types of crusts are related to the minerals associated with each genetic process. Fe-vernadite concentrates essentially Co, Ce and Ni, whereas the buserite, intergrown with asbolane, concentrates Ni and Cu, controlling the enrichment in strategic elements of the two-end member crusts. Therefore, the bright lamination of buserite/asbolane leads to enrichment in Mn, Ni and Cu, whereas hydrogenetic laminae of Fe-vernadite contribute to increasing the contents of Fe (up to 30 wt %), Co and Ce, reaching the highest enrichments in layers with very low growth rates. In this way, the mixed hydrogenetic/diagenetic crust (DR07-08) is enriched in Ni and Cu and the purely hydrogenetic crust (DR16-13) in Co and Ce.
- (5) The enrichment in REYs for the Mn-oxide phase is clearly evidenced by the purely hydrogenetic crust. Moreover, the enrichment in HREEs, related to Fe-hydroxides, is confirmed in the two types of crusts. An important positive anomaly of Ce is depicted higher in the Mn-oxide than the Fe-oxyhydroxide phases. A prominent negative anomaly in Y, depicted for the Fe-oxyhydroxide phases by [94], is also shown in the CISP crusts, but not in the Mn-oxide phases, corresponding to the diagenetic/hydrogenetic crusts.
- (6) At least one episode of enrichment in critical metals (Co, Ni) has been derived for both crusts between 29 and 22 Ma that might be extrapolated to all the CISP. Other episodes of metal-rich mineralization have taken place on the Tropic Seamount crust between 99 and 84 Ma. We suggest that these enrichment episodes in critical metals might be related to expansion events of the OMZ in the Eastern Atlantic Ocean.
- (7) Enrichment in critical metals might be explained by several factors controlling the type of hydrogenetic or diagenetic growth of the crusts: (i) Expansion of the OMZ in the Atlantic Ocean caused by global oceanographic/climate changes, that will promote slow growth of hydrogenetic Fe–Mn oxide minerals enriched in Co, Tl and Ce; (ii) Local factors such as micro-topography and increases in undercurrent strengths bathing the seamounts, that will produce erosion and/or sediment deposition, and thus rapid growth of diagenetic Mn-oxide laminations enriched in Cu and Ni; (iii) Early phosphatization when the OMZ was intensified and expanded, promoting

the formation of CFA enriched in Y and P, in propitious layers enriched in carbonate sediments within the crusts.

We can conclude that these high-resolution studies represent an important tool not only to enhance our knowledge of the different genetic processes, but also to identify the influence of local, regional or global changes in mass-water chemistry, element inputs and environmental factors affecting the crust growth. The high-resolution analyses of Fe–Mn crusts have evidenced that the type of genetic processes directly determined the mineralogy of crusts and, furthermore, the enrichment in critical elements such as Co, Ni, Cu and REYs.

Supplementary Materials: The following are available online at <http://www.mdpi.com/2075-163X/8/7/285/s1>, Table S1: EPMA spot analysis from Figure 10. All the data are in percentage, Table S2: Mineral phases recognised with EPMA spot and layer-by-layer analysis, Table S3: Set of all layer-by-layer and spot analysis obtained in studied crusts by EPMA.

Author Contributions: Marine Geology Dv., Geological Survey of Spain (IGME) provided the samples for this work; E.M. and F.J.G. conceived and designed the experimental research; E.M. performed the experiments, analysed the data and wrote the paper; F.J.G., L.S., T.M. and R.L. substantially revised the work. J.R., E.B. and M.C.-C. have performed and revised all the geochemical analysis. The authors have approved the submitted version and agree to be personally accountable for the author's own contributions and for ensuring that questions related to the accuracy or integrity of any part of the work, even ones in which the author was not personally involved, are appropriately investigated, resolved, and documented in the literature.

Acknowledgments: This research is funded by the EXPLOSEA project (CTM2016-75947-R) of the Secretary of State for Research and Innovation (SEIDI-MINEICO) of Spain. Data for this paper has been collected in the framework of the Project for the Spanish Extension of the Continental Shelf according the United Nations for Convention of the Law of the Sea (UNCLOS). The work was also supported by the Spanish projects SUBVENT (CGL2012-39524-C02), the Extension of the Continental Shelf of Spain project (CTM2010-09496-E), IGME project REMIMARES (IGME-2571); and European projects EMODnet-Geology (EASME/EMFF/2016/1.31.2-Lot 1/SI2.750862) and H2020 GeoERA-MINDeSEA project (Grant Agreement No. 731166, project GeoE.171.001). Egidio Marino would also like to thank the Ministry of Education, Culture and Sport for its FPU scholarship (FPU014/06774). The staff of the “Centro Nacional de Microscopía Electrónica” and the Laboratories of Crystallography and Mineralogy Department (Geology Faculty) of the Complutense University of Madrid (UCM), and the Laboratories of the Geological Survey of Spain (IGME) are also thanked for allowing us to use their facilities. We thank the two anonymous Reviewers and Editors for comments that helped improve this paper.

Conflicts of Interest: The authors declare no conflict of interest. The founding sponsors had no role in the design of the study; in the collection, analyses, or interpretation of data; in the writing of the manuscript, and in the decision to publish the results.

References

1. International Seabed Authority (ISA). 2018. Available online: <https://www.isa.org.jm> (accessed on 11 January 2018).
2. Halbach, P.; Hebisch, U.; Scherhag, C. Geochemical variations of ferromanganese nodules and crusts from different provinces of the Pacific Ocean and their genetic control. *Chem. Geol.* **1981**, *34*, 3–17. [CrossRef]
3. Hein, J.R.; Morgenson, L.A.; Clague, D.A.; Koski, A. Cobalt-rich ferromanganese crusts from the Exclusive Economic Zone of the United States and nodules from the oceanic Pacific. In *Geology and Resource Potential of the Continental Margin of Western North America and Adjacent Ocean Basins-Beaufort Sea to Baja California*; Scholl, D.W., Grantz, A., Vedder, J.G., Eds.; Circum-Pacific Council for Energy and Mineral Resources: Washington, DC, USA, 1987; pp. 753–771.
4. Hein, J.R.; Schwab, W.C.; Davis, A. Cobalt- and platinum-rich ferromanganese crusts and associated substrate rocks from the Marshall Islands. *Mar. Geol.* **1988**, *78*, 255–283. [CrossRef]
5. Baturin, G.N. *The Geochemistry of Manganese and Manganese Nodules in the Ocean*; Springer: Dordrecht, The Netherlands, 1988, ISBN 978-94-009-3731-4.
6. Hein, J.R.; Koschinsky, A.; Bau, M.; Manheim, F.T.; Kang, J.K.; Roberts, L. Co-rich ferromanganese crusts in the Pacific. In *Handbook of Marine Mineral Deposits*; CRC Marine Science Series; Cronan, D.S., Ed.; CRC Press: Boca Raton, FL, USA, 2000; pp. 239–279.
7. Hein, J.R.; Conrad, T.A.; Staudigel, H. Seamount mineral deposits: A source of rare metals for high technology industries. *Oceanography* **2010**, *23*, 184–189. [CrossRef]

8. Hein, J.R.; Mizell, K.; Koschinsky, A.; Conrad, T.A. Deep-ocean mineral deposits as a source of critical metals for high- and green-technology applications: Comparison with land-based resources. *Ore Geol. Rev.* **2013**, *51*, 1–14. [\[CrossRef\]](#)
9. Hein, J.R.; Spinardi, F.; Okamoto, N.; Mizell, K.; Thorburn, D.; Tawake, A. Critical metals in manganese nodules from the Cook Islands EEZ, abundance and distributions. *Ore Geol. Rev.* **2015**, *68*, 97–116. [\[CrossRef\]](#)
10. Hein, J.R.; Conrad, T.; Mizell, K.; Banakar, V.K.; Frey, F.A.; Sager, W.W. Controls on ferromanganese crust composition and reconnaissance resource potential, Ninetyeast Ridge, Indian Ocean. *Deep-Sea Res. Part 1* **2016**, *110*, 1–19. [\[CrossRef\]](#)
11. Muiños, S.B.; Hein, J.R.; Frank, M.; Monteiro, J.H.; Gaspar, L.; Conrad, T.; Pereira, H.G.; Abrantes, F. Deep-sea Fe–Mn crusts from the northeast Atlantic Ocean: Composition and resource considerations. *Mar. Georesour. Geotechnol.* **2013**, *31*, 40–70. [\[CrossRef\]](#)
12. Hein, J.R.; Koschinsky, A. Deep-Ocean Ferromanganese Crusts and Nodules. *Treatise Geochem.* **2014**, *13*, 273–291.
13. González, F.J.; Somoza, L.; Hein, J.R.; Vázquez, J.T.; Medialdea, T.; León, R.; Martín Rubí, J.A.; Bellido, E.; Reyes, J. Deep-water seamounts and banks along the Atlantic Spanish continental margin as a potential source of raw materials. *Eur. Mineral. Conf.* **2012**, *1*, EMC2012-422.
14. González, F.J.; Somoza, L.; Hein, J.R.; Medialdea, T.; León, R.; Urgorri, V.; Reyes, J.; Martín-Rubí, J.A. Phosphorites, Co-rich Mn nodules, and Fe–Mn crusts from Galicia Bank, NE Atlantic: Reflections of Cenozoic tectonics and paleoceanography. *Geochem. Geophys. Geosyst.* **2016**, *17*, 346–374. [\[CrossRef\]](#)
15. Hein, J.R.; Koschinsky, A.; Halbach, P.; Manheim, F.T.; Bau, M.; Kang, J.K.; Lubick, N. Iron and manganese oxide mineralization in the Pacific. *Geol. Soc. Lond. Spec. Publ.* **1997**, *119*, 123–138. [\[CrossRef\]](#)
16. Węgorzewski, A.V.; Kuhn, T. The influence of suboxic diagenesis on the formation of manganese nodules in the Clarion Clipperton nodule belt of the Pacific Ocean. *Mar. Geol.* **2014**, *357*, 123–138. [\[CrossRef\]](#)
17. Węgorzewski, A.V.; Kuhn, T.; Dohrmann, R.; Wirth, R.; Grangeon, S. Mineralogical characterization of individual growth structures of Mn-nodules with different Ni + Cu content from the central Pacific Ocean. *Am. Mineral.* **2015**, *100*, 2497–2508. [\[CrossRef\]](#)
18. Kuhn, T.; Węgorzewski, A.; Rühlemann, C.; Vink, A. Composition, formation, and occurrence of polymetallic nodules. In *Deep-Sea Mining: Resource Potential, Technical and Environmental Considerations*; Sharma, R., Ed.; Springer International Publishing: Cham, Switzerland, 2017; pp. 23–63, ISBN 978-3-319-52557-0.
19. Hodkinson, R.A.; Stoffers, P.; Scholten, J.; Cronan, D.S.; Jeschke, G.; Rogers, T.D.S. Geochemistry of hydrothermal manganese deposits from the Pitcairn Island hotspot, southeastern Pacific. *Geochim. Cosmochim. Acta* **1994**, *58*, 5011–5029. [\[CrossRef\]](#)
20. Nath, N.; Plüger, W.; Roelandts, I. Geochemical constraints on the hydrothermal origin of ferromanganese encrustations from the Rodrigues Triple Junction, Indian Ocean. *Geol. Soc. Lond. Spec. Publ.* **1997**, *119*, 199–212. [\[CrossRef\]](#)
21. Kuhn, T.; Bau, M.; Blum, N.; Halbach, P. Origin of negative Ce anomalies in mixed hydrothermal–hydrogenetic Fe–Mn crusts from the Central Indian Ridge. *Earth Planet. Sci. Lett.* **1998**, *163*, 207–220. [\[CrossRef\]](#)
22. Dekov, V.M.; Savelli, C. Hydrothermal activity in the SE Tyrrhenian Sea: An over-view of 30 years of research. *Mar. Geol.* **2004**, *204*, 161–185. [\[CrossRef\]](#)
23. Hein, J.R. Cobalt-rich ferromanganese crusts. Global distribution, composition, origin and research activities. In *Workshop on Minerals Other than Polymetallic Nodules of the International Seabed Area*; International Seabed Authority: Kingston, Jamaica, 2004; pp. 188–256.
24. Halbach, P.; Segl, M.; Puteanus, D.; Mangini, A. Co-fluxes and growth rates in ferromanganese deposits from central Pacific seamount areas. *Nature* **1983**, *304*, 716–719. [\[CrossRef\]](#)
25. Rona, P.A. The changing vision of marine minerals. *Ore Geol. Rev.* **2008**, *33*, 618–666. [\[CrossRef\]](#)
26. González, F.J.; Somoza, L.; Lunar, R.; Martínez-Frías, J.; Medialdea, T.; León, R.; Martín-Rubí, J.A.; Torres, T.; Ortiz, J.E.; Marino, E. Polymetallic ferromanganese deposits research on the Atlantic Spanish continental margin. In Proceedings of the 43rd Underwater Mining Institute Conference, Lisboa, Portugal, 21–28 September 2014; Hein, J.R., Barriga, F.J.A.S., Morgan, C.L., Eds.
27. Marino, E.; González, F.J.; Somoza, L.; Lunar, R.; Ortega, L.; Vázquez, J.T.; Reyes, J.; Bellido, E. Strategic and rare elements in Cretaceous–Cenozoic cobalt-rich ferromanganese crusts from seamounts in the Canary Island Seamount Province (northeastern tropical Atlantic). *Ore Geol. Rev.* **2017**, *87*, 41–61. [\[CrossRef\]](#)

28. European Commission. 2018. Available online: <https://ec.europa.eu/> (accessed on 6 February 2018).
29. Minerals for EU Project. 2018. Available online: <http://www.minerals4eu.eu/> (accessed on 6 February 2018).
30. Han, X.; Jin, X.; Yang, S.; Fietzke, J.; Eisenhauer, A. Rhythmic growth of Pacific ferromanganese nodules and their Milankovitch climatic origin. *Earth Planet. Sci. Lett.* **2003**, *211*, 143–157. [[CrossRef](#)]
31. Oda, H.; Usui, A.; Miyagi, I.; Joshima, M.; Weiss, B.P.; Shantz, C.; Fong, L.E.; McBride, K.K.; Harder, R.; Baudenbacher, F.J. Ultrafine-scale magnetostratigraphy of marine ferromanganese crust. *Geology* **2011**, *39*, 227–230. [[CrossRef](#)]
32. González, F.J.; Somoza, L.; León, R.; Medialdea, T.; de Torres, T.; Ortiz, J.E.; Lunar, R.; Martínez-frías, J.; Merinero, R. Ferromanganese nodules and microhardgrounds associated with the Cadiz Contourite Channel (NE Atlantic): Palaeoenvironmental records of fluid venting and bottom currents. *Chem. Geol.* **2012**, *310*–311, 56–78. [[CrossRef](#)]
33. Usui, A.; Nishi, K.; Sato, H.; Nakasato, Y.; Thornton, B.; Kashiwabara, T.; Tokumaru, A.; Sakaguchi, A.; Yamaoka, K.; Kato, S.; et al. Continuous growth of hydrogenetic ferromanganese crusts since 17 Myr ago on Takuyo-Daigo Seamount, NW Pacific, at water depths of 800–5500 m. *Ore Geol. Rev.* **2017**, *87*, 71–87. [[CrossRef](#)]
34. Konstantinova, N.; Cherkashov, G.; Hein, J.R.; Mirão, J.; Dias, L.; Madureira, P.; Kuznetsov, V.; Maksimov, F. Composition and characteristics of the ferromanganese crusts from the western Arctic Ocean. *Ore Geol. Rev.* **2017**, *87*, 88–99. [[CrossRef](#)]
35. Carracedo, J.C.; Day, S.J.; Guillou, H.; Rodríguez Badiola, E.; Canas, J.A.; Pérez Torrado, F.J. Hotspot volcanism close to a passive continental margin: The Canary Islands. *Geol. Mag.* **1998**, *135*, 591–604. [[CrossRef](#)]
36. Geldmacher, J.; Hoernle, K.; Bogaard, P.v.d.; Duggen, S.; Werner, R. New ⁴⁰Ar/³⁹Ar age and geochemical data from seamounts in the Canary and Madeira Volcanic Provinces: A contribution to the “Great Plume Debate”. *Earth Planet. Sci. Lett.* **2005**, *237*, 85–101. [[CrossRef](#)]
37. Geldmacher, J.; Hoernle, K.; Hanan, B.B.; Blichert-Toft, J.; Hauff, F.; Gill, J.B.; Schmincke, H.-U. Hafnium isotopic variations in East Atlantic intraplate volcanism. *Contrib. Mineral. Petrol.* **2011**, *162*, 21–36. [[CrossRef](#)]
38. Hoernle, K.; Schmincke, H.U. The role of partial melting in the 15-Ma geochemical evolution of Gran Canaria: A blob model for the Canary Hotspot. *J. Petrol.* **1993**, *34*, 599–626. [[CrossRef](#)]
39. Van den Bogaard, P. The origin of the Canary Island Seamount Province—New ages of old Seamounts. *Sci. Rep.* **2013**, *3*, 2107. [[CrossRef](#)] [[PubMed](#)]
40. Carracedo, J.C.; Pérez-Torrado, F.J.; Ancochea, E.; Meco, J.; Hernán, F.; Cubas, C.R.; Casillas, R.; Rodríguez Badiola, E.; Ahijado, A. Cenozoic volcanism II: The Canary Islands. In *The Geology of Spain*; Gibbons, E., Moreno, M.T., Eds.; Geological Society: London, UK, 2002; pp. 439–472.
41. Ancochea, E. Evolución de la actividad volcánica. In *Geología de España*; Vera, J.A., Ed.; SGE-IGME: Madrid, Spain, 2004; pp. 639–641.
42. Schmincke, H.-U.; Krastel, S.; Hansteen, T.; Sumita, M. Preliminary Results, Leg M43/1, Rock Sampling and Description. In *DECOS/OMEX II, Cruise No. 43*; Schmincke, H.-U., Graf, G., Eds.; METEOR-Berichte: Hamburg, Germany, 2000; p. 99.
43. Instituto Geológico y Minero de España (IGME). Presentación Parcial de Datos e Información Sobre los Límites de la Plataforma Continental de España al Oeste de las Islas Canarias, Conforme a la Parte VI y el Anexo II de la Convención de las Naciones Unidas sobre el Derecho del Mar. 2015. Unpublished work. 2015.
44. Koschinsky, A.; Halbach, P. Sequential leaching of marine ferromanganese precipitates: Genetic implications. *Geochim. Cosmochim. Acta* **1995**, *59*, 5113–5132. [[CrossRef](#)]
45. González, F.J.; Rincón-Tomás, B.; Somoza, L.; Hein, J.R.; Medialdea, T.; Madureira, P.; Reyes, J.; Hoppert, M.; Reitner, J. Fe-rich mineralized microbes from hydrothermal vents at Tagoro submarine volcano, El Hierro Island (central east Atlantic). In Proceedings of the Geological Society of America 113th Annual Meeting, Honolulu, HI, USA, 23–25 May 2017; Volume 49, p. 4. [[CrossRef](#)]
46. Somoza, L.; González, F.J.; Barker, S.J.; Madureira, P.; Medialdea, T.; de Ignacio, C.; Lourenço, N.; León, R.; Vázquez, J.T.; Palomino, D. Evolution of submarine eruptive activity during the 2011–2012 El Hierro event as documented by hydroacoustic images and remotely operated vehicle observations. *Geochem. Geophys. Geosyst.* **2017**, *18*, 3109–3137. [[CrossRef](#)]

47. Machín, F.; Hernández-Guerra, A.; Pelegrí, J.L. Mass fluxes in the Canary Basin. *Prog. Oceanogr.* **2006**, *70*, 416–447. [\[CrossRef\]](#)
48. Pastor, M.V.; Vélez-Belchí, P.; Hernández-Guerra, A. Water masses in the Canary current large marine ecosystem. In *Oceanographic and Biological Features in the Canary Current Large Marine Ecosystem, Proceedings of the IOC/UNESCO 2015, 18–25 June, Paris, France*; Valdés, L., Déniz-González, I., Eds.; IOC Technical Series 115; UNESCO: Paris, France, 2015; pp. 73–79.
49. Sarnthein, M.; Thiede, J.; Pflaumann, U.; Erlenkeuser, H.; Fütterer, D.; Koopmann, B.; Lange, H.; Seibold, E. Atmospheric and oceanic circulation patterns off northwest Africa during the past 25 million years. In *Geology of Northwest Africa Continental Margin*; von Rad, U., Hinz, K., Sarnthein, M., Seibold, E., Eds.; Springer: Berlin/Heidelberg, Germany; New York, NY, USA, 1982; pp. 545–604.
50. Hernández-Guerra, A.; Fraile-Nuez, E.; López-Laatzén, F.; Martínez, A.; Parrilla, G.; Vélez-Belchí, P. Canary current and north equatorial current from an inverse box model. *J. Geophys. Res.* **2005**, *110*, C12019. [\[CrossRef\]](#)
51. Knoll, M.; Hernández-Guerra, A.; Lenz, B.; López-Laatzén, F.; Machín, F.; Müller, T.; Siedler, G. The Eastern Boundary Current system between the Canary Islands and the African coast. *Deep Sea Res. Part II* **2002**, *19*, 3427–3440. [\[CrossRef\]](#)
52. Mémerly, L.; Arhan, M.; Alvarez-Salgado, X.A.; Messias, M.-J.; Mercier, H.; Castro, C.G.; Rios, A.F. The water masses along the western boundary of the south and equatorial Atlantic. *Prog. Ocean.* **2000**, *47*, 69–98. [\[CrossRef\]](#)
53. Brandt, P.; Hormann, V.; Körtzinger, A.; Visbeck, M.; Krahmann, G.; Stramma, L.; Lumpkin, R.; Schmid, C. Changes in the ventilation of the oxygen minimum zone of the tropical North Atlantic. *J. Phys. Oceanogr.* **2010**, *40*, 1784–1801. [\[CrossRef\]](#)
54. Brandt, P.; Greatbatch, R.J.; Claus, M.; Didwischus, S.-H.; Hormann, V.; Funk, A.; Hahn, J.; Krahmann, G.; Fischer, J.; Körtzinger, A. Ventilation of the equatorial Atlantic by the equatorial deep jets. *Phys. Oceanogr. Oceans* **2012**, *117*, C12015. [\[CrossRef\]](#)
55. Bashmachnikov, I.; Nascimento, Â.; Neves, F.; Menezes, T.; Koldunov, N.V. Distribution of intermediate water masses in the subtropical northeast Atlantic. *Ocean Sci.* **2015**, *11*, 803–827. [\[CrossRef\]](#)
56. Helmers, E.; Schrems, O. Wet deposition of metals to the tropical North and the South Atlantic ocean. *Atmos. Environ.* **1995**, *29*, 2475–2484. [\[CrossRef\]](#)
57. Eltayeb, M.A.H.; Injuk, J.; Manhaut, W.; Van Grieken, R.E. Elemental Composition of mineral aerosol generated from Sudan Sahara Sand. *J. Atmos. Chem.* **2001**, *40*, 247–273. [\[CrossRef\]](#)
58. Bristow, C.S.; Hudson-Edwards, K.A.; Chappell, A. Fertilizing the Amazon and equatorial Atlantic with West African dust. *Geophys. Res. Lett.* **2010**, *37*. [\[CrossRef\]](#)
59. Palomino, D.; Vázquez, J.-T.; Somoza, L.; León, R.; López-González, N.; Medialdea, T.; Fernández-Salas, L.-M.; González, F.-J.; Rengel, J.A. Geomorphological features in the southern Canary Island volcanic province: The importance of volcanic processes and massive slope instabilities associated with seamounts. *Geomorphology* **2016**, *255*, 125–139. [\[CrossRef\]](#)
60. Golden, D.C.; Chen, C.C.; Dixon, J.B. Transformation of birnessite to buserite, todorokite, and manganite under mild hydrothermal treatment. *Clays Clay Min.* **1987**, *35*, 271. [\[CrossRef\]](#)
61. Tessier, A.P.; Campbell, P.G.C.; Bisson, M.X. Sequential Extraction Procedure for the Speciation of Trace Metals. *Anal. Chem.* **1979**, *51*, 844–851. [\[CrossRef\]](#)
62. Manheim, F.T.; Lane-Bostwick, C.M. Cobalt in ferromanganese crusts as a monitor of hydrothermal discharge on the Pacific sea floor. *Nature* **1988**, *335*, 59–62. [\[CrossRef\]](#)
63. Hein, J.R.; Schulz, M.S.; Kang, J.-K. Insular and submarine ferromanganese mineralization of the Tonga-Lau region. *Mar. Min.* **1990**, *9*, 305–354.
64. Kustova, G.N.; Burgina, E.B.; Sadykov, V.A.; Poryvaev, S.G. Vibrational spectroscopic investigation of the goethite thermal decomposition products. *Phys. Chem. Miner.* **1992**, *18*, 379–382. [\[CrossRef\]](#)
65. Ruan, H.D.; Frost, R.L.; Klopogge, J.T.; Duong, L. Infrared spectroscopy of goethite dehydroxylation: III. FT-IR microscopy of in situ study of the thermal transformation of goethite to hematite. *Spectrochim. Acta Part A Mol. Biomol. Spectrosc.* **2002**, *58*, 967–981. [\[CrossRef\]](#)
66. Saito, G.; Kunisada, Y.; Nomura, T.; Sakaguchi, N.; Akiyama, T. Twin formation in hematite during dehydration of goethite. *Phys. Chem. Miner.* **2016**, *43*, 749–757. [\[CrossRef\]](#)
67. Rudnick, R.L.; Gao, S. Composition of the Continental Crust. In *Treatise on Geochemistry*, 2nd ed.; Holland, H.D., Turekian, K.K., Eds.; Elsevier: Oxford, UK, 2014; pp. 1–51.

68. Taylor, S.R.; McLennan, S.M. *The Continental Crust; Its Composition and Evolution; An Examination of the Geochemical Record Preserved in Sedimentary Rocks*; Blackwell: Oxford, UK, 1985.
69. Koschinsky, A.; Hein, J.R. Uptake of elements from seawater by ferromanganese crusts: Solid-phase associations and seawater speciation. *Mar. Geol.* **2003**, *198*, 331–351. [[CrossRef](#)]
70. Baturin, G.N.; Dubinchuk, V.T. Mineralogy and chemistry of ferromanganese crusts from the Atlantic Ocean. *Geochim. Int.* **2011**, *49*, 578–593. [[CrossRef](#)]
71. Baturin, G.N.; Dubinchuk, V.T.; Rashidov, V.A. Ferromanganese crusts from the Sea of Okhotsk. *Oceanology* **2012**, *52*, 88–100. [[CrossRef](#)]
72. Bonatti, E.; Kraemer, T.; Rydell, H. Classification and genesis of submarine ironmanganese deposits. In *Ferromanganese Deposits of the Ocean Floor*; Horn, D.R., Ed.; Arden House: New York, NY, USA, 1972; pp. 149–165.
73. Josso, P.; Pelleter, E.; Pourret, O.; Fouquet, Y.; Etoubleau, J.; Cheron, S.; Bollinger, C. A new discrimination scheme for oceanic ferromanganese deposits using high field strength and rare earth elements. *Ore Geol. Rev.* **2017**, *87*, 3–15. [[CrossRef](#)]
74. Bau, M.; Schmidt, K.; Koschinsky, A.; Hein, J.; Kuhn, T.; Usui, A. Discriminating between different genetic types of marine ferro-manganese crusts and nodules based on rare earth elements and yttrium. *Chem. Geol.* **2014**, *381*, 1–9. [[CrossRef](#)]
75. Puteanus, D.; Halbach, P. Correlation of Co concentration and growth rate—A method for age determination of ferromanganese crusts. *Chem. Geol.* **1988**, *69*, 73–85. [[CrossRef](#)]
76. Hein, J.R.; Yeh, H.-W.; Gunn, S.H.; Sliter, W.V.; Benninger, L.M.; Wang, C.-H. Two major Cenozoic episodes of phosphogenesis recorded in equatorial Pacific seamount deposits. *Paleoceanography* **1993**, *8*, 293–311. [[CrossRef](#)]
77. Koschinsky, A.; Stascheit, A.; Bau, M.; Halbach, P. Effects of phosphatization on the geochemical and mineralogical composition of marine ferromanganese crusts. *Geochim. Cosmochim. Acta* **1997**, *61*, 4079–4094. [[CrossRef](#)]
78. Hyeong, K.; Kim, J.; Yoo, C.M.; Moon, J.-W.; Seo, I. Cenozoic history of phosphogenesis recorded in the ferromanganese crusts of central and western Pacific seamounts: Implications for deepwater circulation and phosphorus budgets. *Palaeogeogr. Palaeoclimatol. Palaeoecol.* **2013**, *392*, 293–301. [[CrossRef](#)]
79. Conrad, T.; Hein, J.R.; Paytan, A.; Clague, D.A. Formation of Fe–Mn crusts within a continental margin environment. *Ore Geol. Rev.* **2017**, *87*, 25–40. [[CrossRef](#)]
80. Henderiks, J. Cocolith Studies in the Canary Basin: Glacial-interglacial Paleooceanography of the Eastern Boundary Current System. Unpublished Ph.D. Thesis, ETH Zürich, Zürich, Switzerland, 2001; p. 175.
81. Frierdich, A.J.; Hasenmueller, E.A.; Catalano, J.G. Composition and structure of nanocrystalline Fe and Mn oxide cave deposits: Implications for trace element mobility in karst systems. *Chem. Geol.* **2011**, *284*, 82–96. [[CrossRef](#)]
82. Lysyuk, G.N. Biomineral nanostructures of manganese oxides in oceanic ferromanganese nodules. *Geol. Ore Depos.* **2008**, *50*, 647–649. [[CrossRef](#)]
83. Reith, F.; Zammit, C.M.; Shar, S.S.; Etschmann, B.; Bottrill, R.; Southam, G.; Ta, C.; Kilburn, M.; Oberthür, T.; Ball, A.S.; et al. Biological role in the transformation of platinum-group mineral grains. *Nat. Geosci.* **2016**, *9*, 294–298. [[CrossRef](#)]
84. Bogdanov, Y.A.; Sorochtin, O.G.; Zonenshain, L.P.; Kuptzov, V.M.; Lisitzina, N.A.; Podrajanski, A.M. *Ferromanganese Crust and Nodules of Pacific Seamounts*; Nauka: Moscow, Russia, 1990; p. 229.
85. Bogdanov, Y.A.; Bogdanova, O.Y.; Dubinin, A.V.; Gorand, A.; Gorshkov, A.I.; Gurvich, E.G.; Isaeva, A.B.; Ivanov, G.V.; Jansa, L.F.; Monaco, A. Composition of ferromanganese crusts and nodules at northwest Pacific guyots and geologic and paleoceanographic considerations. In *Proceedings of the Ocean Drilling Program: Scientific Results 144*; Haggerty, J.A., Premoli Silva, I., Rack, F.R., McNutt, M.K., Eds.; Ocean Drilling Program: College Station, TX, USA, 1995; p. 1059.
86. Bogdanova, O.Y.; Gorshkov, A.I.; Novikov, G.V.; Bogdanov, Y.A. Mineralogy of morphogenetic types of ferromanganese deposits in the world ocean. *Geol. Ore Depos.* **2008**, *50*, 462–469. [[CrossRef](#)]
87. Post, J.E. Manganese oxide minerals: Crystal structures and economic and environmental significance. *Proc. Natl. Acad. Sci. USA* **1999**, *96*, 3447–3454. [[CrossRef](#)] [[PubMed](#)]

88. Cui, H.; Feng, X.; Tan, W.; He, J.; Hu, R.; Liu, F. Synthesis of todorokite-type manganese oxide from Cu-buserite by controlling the pH at atmospheric pressure. *Microporous Mesoporous Mater.* **2009**, *117*, 41–47. [\[CrossRef\]](#)
89. Feng, X.; Zhu, M.; Ginder-Vogel, M.; Ni, C.; Parikh, S.J.; Sparks, D.L. Formation of nano-crystalline todorokite from biogenic Mn oxides. *Geochim. Cosmochim. Acta* **2010**, *74*, 3232–3245. [\[CrossRef\]](#)
90. Feng, X.; Zhao, H.; Liu, F.; Cui, H.; Tan, W.; Li, W. Transformation from Phylломanganates to Todorokite under Various Conditions: A Review of Implication for Formation Pathway of Natural Todorokite. In *Advances in the Environmental Biogeochemistry of Manganese Oxides*; ACS Symposium Series 2016; American Chemical Society: Washington, DC, USA, 2016; Volume 1197.
91. Manceau, A.; Lanson, M.; Takahashi, Y. Mineralogy and crystal chemistry of Mn, Fe, Co, Ni, and Cu in a deep-sea Pacific polymetallic nodule. *Am. Mineral.* **2014**, *99*, 2068–2083. [\[CrossRef\]](#)
92. Koschinsky, A.; van Gerven, M.; Halbach, P. First discovery and investigation of massive ferromanganese crusts in the NE Atlantic in comparison to hydrogenetic Pacific occurrences. *Mar. Georesour. Geotechnol.* **1995**, *13*, 375–391. [\[CrossRef\]](#)
93. Koschinsky, A.; Halbach, P.; Hein, J.R.; Mangini, A. Ferromanganese crusts as indicators for paleoceanographic events in the NE Atlantic. *Geol. Rundschau* **1996**, *85*, 567–576. [\[CrossRef\]](#)
94. Bau, M.; Koschinsky, A. Oxidative scavenging of cerium on hydrous Fe oxide: Evidence from the distribution of rare earth elements and yttrium between Fe oxides and Mn oxides in hydrogenetic ferromanganese crusts. *Geochem. J.* **2009**, *43*, 37–47. [\[CrossRef\]](#)
95. Chukhrov, F.V.; Gorshkov, A.I.; Vitovskaya, I.V.; Drits, V.A.; Sivtsov, A.I.; Rudnitskaya, E.S. Crystallochemical nature of Co-Ni asbolan. *Izvestia Akademii Nauk, SSSR. Seriya Geol.* **1982**, *6*, 73–81.
96. Chukhrov, F.V.; Gorshkov, A.I.; Drits, V.A.; Shterenberg, A.V.; Sakharov, B.A. Mixed-layer asbolan-buserite minerals and asbolans in oceanic iron-manganese concretions. *Int. Geol. Rev.* **1983**, *25*, 838–847.
97. Moffett, J.W. Microbially mediated cerium oxidation in sea water. *Nature* **1990**, *345*, 421–423. [\[CrossRef\]](#)
98. Sholkovitz, E.R.; Shaw, T.J.; Schneider, D.L. The geochemistry of rare earth elements in the seasonally anoxic water column and porewaters of Chesapeake Bay. *Geochim. Cosmochim. Acta* **1992**, *56*, 3389–3402. [\[CrossRef\]](#)
99. Newman, H.R. The mineral industries of Morocco and Western Sahara U.S. In *Geological Survey Minerals Yearbook V. III*; U.S. Government Publishing Office (OGP): Pittsburgh, PA, USA, 2011; p. 10.
100. Wang, X.; Peine, F.; Schmidt, A.; Schröder, H.C.; Wiens, M.; Schloßmacher, U.; Müller, W.E.G. Concept of Biogenic Ferromanganese Crust Formation: Coccoliths as Bio-seeds in Crusts from Central Atlantic Ocean (Senghor Seamount/Cape Verde). *Nat. Prod. Commun.* **2011**, *6*, 1–10.
101. Manceau, A.; Gorshkov, A.I.; Drits, V.A. Structural chemistry of Mn, Fe, Co, and Ni in manganese hydrous oxides: Part II. Information from EXAFS spectroscopy and electron and X-ray diffraction. *Am. Mineral.* **1992**, *77*, 1144–1157.
102. Varentsov, I.M.; Drits, V.A.; Gorshkov, A.I.; Sivtsov, A.V.; Sakharov, B.A. Mn-Fe oxyhydroxide crusts from Krylov Seamount (Eastern Atlantic): Mineralogy, geochemistry and genesis. *Mar. Geol.* **1991**, *96*, 53–70. [\[CrossRef\]](#)
103. Morel, F.M.M.; Milligan, A.J.; Saito, M.A. Marine bioinorganic chemistry: The role of trace metals in the oceanic cycles of major nutrients. *Treatise Geochem.* **2003**, 113–143. [\[CrossRef\]](#)
104. Vance, D.; Archer, C.; Little, S.H.; Köbberich, M.; de Souza, G.F. The oceanic cycles of the transition metals and their isotopes. *Acta Geochim.* **2017**, *36*, 359–362. [\[CrossRef\]](#)
105. De Carlo, E.H.; McMurtry, G.M.; Kim, K.H. The geochemistry of ferromanganese crusts from the Hawaiian Archipelago-I. Northern survey areas. *Deep-Sea Res. Part A Oceanogr. Res. Pap.* **1987**, *34*, 441–467. [\[CrossRef\]](#)
106. Burns, V.M.; Burns, R.G. Post-depositional metal enrichment processes inside manganese nodules from the north equatorial Pacific. *Earth Planet. Sci. Lett.* **1978**, *39*, 341–348. [\[CrossRef\]](#)
107. Mohwinkel, D.; Kleint, C.; Koschinsky, A. Phase associations and potential selective extraction methods for selected high-tech metals from ferromanganese nodules and crusts with siderophores. *Appl. Geochem.* **2014**, *43*, 13–21. [\[CrossRef\]](#)
108. Moorby, S.A.; Cronan, D.S. The distribution of elements between co-existing phases in some marine ferromanganese-oxide deposits. *Geochim. Cosmochim. Acta* **1981**, *45*, 1855–1877. [\[CrossRef\]](#)
109. Kashiwabara, T.; Takahashi, Y.; Tanimizu, M. A XAFS study on the mechanism of isotopic fractionation of molybdenum during its adsorption on ferromanganese oxides. *Geochem. J.* **2009**, *43*, 31–36. [\[CrossRef\]](#)

110. Kashiwabara, T.; Takahashi, Y.; Marcus, M.A.; Uruga, T.; Tanida, H.; Terada, Y.; Usui, A. Tungsten species in natural ferromanganese oxides related to its different behavior from molybdenum in oxic ocean. *Geochim. Cosmochim. Acta* **2013**, *106*, 364–378. [[CrossRef](#)]
111. De Carlo, E.H.; Wen, X.-Y. The influence of redox reactions on the uptake of dissolved ce by suspended Fe and Mn oxide particles. *Aquat. Geochem.* **1998**, *3*, 357–389. [[CrossRef](#)]
112. Moffett, J.W. The relationship between cerium and manganese oxidation in the marine environment. *Limnol. Oceanogr.* **1994**, *39*, 1309–1318. [[CrossRef](#)]
113. Bau, M. Scavenging of dissolved yttrium and rare earths by precipitating iron oxyhydroxide: Experimental evidence for Ce oxidation, Y-Ho fractionation, and lanthanide tetrad effect. *Geochim. Cosmochim. Acta* **1999**, *63*, 67–77. [[CrossRef](#)]



© 2018 by the authors. Licensee MDPI, Basel, Switzerland. This article is an open access article distributed under the terms and conditions of the Creative Commons Attribution (CC BY) license (<http://creativecommons.org/licenses/by/4.0/>).